# Chaotic Behavior of Rayleigh-Bénard Convection with Shear Flow: Comparison Analysis of Three Components Lorenz Model and Five Components Model

Aoyagi, Takashi
Interdisciplinary Graduate School of Engineering Sciences, Kyushu University

Yagi, Masatoshi
Research Institute for Applied Mechanics, Kyushu University

Itoh, Sanae-I.
Research Institute for Applied Mechanics, Kyushu University

https://doi.org/10.5109/6786348

出版情報：Reports of Research Institute for Applied Mechanics. 43 (115), pp.1-56, 1997-09. 九州大学応用力学研究所

Reports of Research Institute for Applied Mechanics
Vol. XLIII No. 115, 1997

# Chaotic Behavior of Rayleigh-Bénard Convection with Shear Flow
## — Comparison Analysis of Three Components Lorenz Model and Five Components Model —

By Takashi AOYAGI[†], Masatoshi YAGI[*] and Sanae-I. ITOH[*]

The three components Lorenz model for Rayleigh-Bénard convection is extended to the five components model taking an autonomous shear flow effect into account. The five components model is numerically solved and analyzed in detail. Based on the Lyapunov exponent analysis, how the introduction of the new degrees of the freedom (the shear flow) changes the chaotic behavior of the solution is examined. The attractors, the time evolutions, the power spectra, the Nusselt number and so on of the five components model are compared with those of the three components model.

It is found that the solutions of both models converge to the same one when the Rayleigh number is small ($r=\gamma_x<140$). When the normalized Rayleigh number exceeds 140, the difference between the three components model and the five components model is observed, i. e., the former has only the periodic solutions, while the latter contains the chaotic solutions. Some examples are shown. The limitation to a model with a few degrees of freedom is discussed.

***Key words***: Lorenz model, Lyapunov exponent, chaos, shear flow, plasma, Scrape Off Layer (SOL)

**Contents**



[†] Interdisciplinary Graduate School of Engineering Sciences, Kyushu University
[*] Research Institute for Applied Mechanics, Kyushu University

## § 1. Introduction

Chaotic dynamics may be said to have started with the work of Henri Poincarê who have studied the problem of the orbit of three celestial bodies experiencing mutual gravitational attraction. It was very surprising that only three variables are required for chaos when it was found. For chaotic systems, the error grows exponentially in time, so that the state of the system is essentially unknown after a very short time. This phenomenon which occurs only when the governing equations are nonlinear, is known as sensitivity to initial conditions. This concept is similar to Heisenberg's uncertainty principle which tells us that we can not measure both the position and the momentum of a particle simultaneously with arbitrary precision in microscopic level.

Much efforts have been made on the research of chaos in a system with a few degrees of freedom. Although the recent development of computer is very rapid and its ability makes it possible to treat a system with a large number of freedom or more realistic models, it is important to understand what is going to occur in a given situation wihtout entering into the particular equations governing the system.

There are important aspects. The first is how we can simplify a system but keep some meaning in it. Let us consider a specific example: Rayleigh-Bênard convection [1], even in a small container where only two convective rolls are present, is governed by the Navier-Stokes equations, which are in general perfectly insoluble. Without simplifications and approximations, the most powerful computers are incapable of providing us with numerical solutions. First approach: we try to make a model by drastically truncating the original equations; this has been done, we have seen, with the Lorenz model [2, 3]. This approach is already extremely rich; but we can simplify further by passing from differential equations to finite difference equations, ending up with two — and even one-dimensional mapping. By doing this we arrive at an extremely simple formation, exploitable by particularly modest computational means, and we succeed in discovering, among other thing, the route to turbulence via period-doubling cascades [4] which is verified perfectly by experiment.

The second point is the idea of universality. As the model is simplified to the extreme, it shows universality, i. e., insensitivity to the details of the model. In other words, it is not only the equation $f(x)=4\mu x(1-x)$ which describes a period-doubling cascade, but rather that almost any nonlinear function of $x$ will do.

According to the above background, we explain the purpose of our study. The main purpose is comparison of chaos in the three components Lorenz model and in the five components modified Lorenz model. Here the five components model has been used to describe the dynamic of Scrape Off Layer (SOL) in tokamak plasmas. Such a model has been also applied to describe Edge Localized Mode (ELM) observed during High confinement mode (H-mode). Without discussing the underlying detailed physics, we analyze both systems based on numerical simulation, compare the Lyapunov exponent with each other and try to find the universality.

This thesis is organized as follows: The Chapter 2 is devoted to a review about the theory and numerical examples of chaos. In Section 2.1 and 2.2, we explain the concept of attractor and give four examples, i. e. the point attractor, the limit cycle, the torus $T^2$ and the chaotic attractor. In Section 2.3, we introduce the Lyapunov exponent as the critical parameter of chaos, where the positive maximum Lyapunov exponent means that the orbit is chaotic, the zero maximum exponent shows that the orbit is periodic, and the negative maximum exponent corresponds to the case where the orbit converges to a fixed point. In Section 2.4, we explain Floquet theory to discuss about the stability criterion of chaos and further consider the bifurcation theory based on this criterion. In Section 2.5, the theory of intermittency is explained according to Ref. [5]. In Section 2.6, starting from Magneto Hydro Dynamics (MHD) model we derive the reduced MHD (RMHD) model assuming the electrostatic perturbations. Then RMHD model is further simplified to the Lorenz model. We discuss the stability analysis around the fixed points of this system. Some numerical results are also shown.

In Chapter 3, we give main results of this thesis. We derive the extended Lorenz model of five components in Section 3.1. In Section 3.2, we examine the chaotic behavior solving the equations of the three components Lorenz model and the extended Lorenz model. We show their chaotic behaviors by using plots on the phase space, the time evolution of variables, the power spectrum and the relation between the Lyapunov exponent and the control parameter (Rayleigh number in this case). The results of the two models are compared. In Section 3.3, we analyze our numerical results based on the theory of intermittency. The type of intermittency is tried to be identified for both the Lorenz model and the five components model.

Summary and discussions are given in Chapter 4.

## § 2. Review

In this chapter, we review an important concept in dynamics of dissipative system such as attractors in the phase space. A defining attribute of an attractor on which the dynamics is chaotic is that it displays exponentially sensitive dependence on initial conditions (chaotic attractor). A convenient indicator of the sensitivity to small orbit perturbations characteristic of chaotic attractors is the Lyapunov exponent, which is also explained. Related to this topic, we are interested in transitions from the regular behavior of the system to the chaotic behavior. Especially, our concern is the intermittent transition to chaos. To characterize the intermittent transition with variation of a system parameter, Floquet's theory is utilized. We will show an example using the Lorenz model.

### 2.1 Attractors

We analyze the evolution of arbitrary dissipative system. The systems are assumed to be deterministic; since they are described by a continuous flow:

$$\frac{d}{dt}\vec{X}(t)=F(\vec{X}(t))$$

where $\vec{X}$ is vector $R^{m}(m\geq 1)$. The function $F$ contains one or several control parameters $\mu$ which express the constraint under investigation. The constraint can be, for example, the Rayleigh number for the Lorenz model. By changing a control parameter, it is possible to alter the behavior of the system. During the observation, the control parameter is kept (or assumed to be) constant. What interests us primarily is the long-term behavior of dissipative systems. When we think about it, we assume that the motion satisfies the condition that the trajectories stay in a bounded volume of the phase space. If the flow is dissipative, then in this finite volume the trajectories converge towards an attractor, a compact set in the phase space which is invariant under the flow or mapping. Our interest will consist of two parts:

— defining the different types of attractors

— cataloging the modes of transition between attractors.

We explain briefly the three simplest attractors.

The point attractor is a solution which is independent of time — that is, a steady state. This situation is completely understood, since the system does not evolve.

A solution which is periodic in time is a limit cycle, characterized by its amplitude and period. Its Fourier spectrum contains a single fundamental frequency and possibly a certain number of harmonics, depending on the form of the oscillations. The solution to the flow can always be expressed as a Fourier series: if the state of the system is known at a given time, one can predict its state at all later times.

A third type of attractor, again relatively simple, is the torus $T^r (r \geq 2)$ which corresponds to a quasi-periodic regime with $r$ independent fundamental frequencies. Here, too, the Fourier spectrum is composed of a set of lines, whose frequencies are linear combinations of the fundamental frequencies. While the solution to the flow cannot generally be put into the form of an ordinary Fourier series, it is still possible to calculate the state of the system starting from an initial condition.

### 2.2 Chaotic Attractors (Strange Attractors)

What kind of attractor is associated with a regime whose Fourier spectrum contains a broad band? Landau conjectured in 1944 [6] if the dimension $r$ of a torus $T^r$ becomes extremely high, intervals of line spectrum become narrow and as a result they become continuous spectrum. But we know this is false mainly from numerical simulations of three-or five-dimensional system. It is to Ruelle and Takens that we owe the break-through in 1971 [7] of having introduced attractors topologically different from the torus, which they named strange attractors, and of having shown that such attractors could be important in physical problems, including hydrodynamic turbulence. The name "strange attractor" refers to their unusual properties, the most crucial being sensitivity to initial conditions (S. I. C). But recently it is no longer strange, so it is called chaotic attractor. By virtue of S. I. C., any two initially close trajectories on the attractor eventually diverge from one another. Their divergence (average over short time intervals) even increases exponentially with time.

We see that two trajectories, at first almost indistinguishable, later have nothing in common after a finite time has passed. The vanishing of the autocorrelation function, the broad band of the Fourier spectrum, and the intrinsic unpredictability of the system are all consequences of S. I. C.. In particular, it is clear that the slightest error or imprecision in specifying the initial condition will prevent us from deciding which will be the trajectory followed by the system, and therefore from making other than a statistical prediction on the long-term future of the system.

For a chaotic solution associated with a chaotic attractor, S. I. C. implies the existence of a positive Lyapunov exponent $\lambda$ [8, 9, 10]. This is a direct consequence of the average divergence of neighboring trajectories. Therefore, finding a positive Lyapunov exponent is an unambiguous signature of a chaotic regime. For that reason, we explain the Lyapunov exponent in the next section.

### 2.3 Lyapunov Exponent

It becomes increasingly difficult to follow the evolution of the chaotic flow as the divergence of the trajectories on the attractor becomes more rapid. This is why we try to estimate or to measure the rate of divergence. The quantity used to characterize the divergence is the *Lyapunov exponent,* sometimes also called the *Lyapunov number.*

To estimate the significance of this quantity, let us examine the behavior of a trajectory initially close to a solution $\vec{\phi}(t)$ of a flow:

$$\frac{d\vec{\phi}}{dt}=F(\vec{\phi}).$$

Without loss of generality, we will limit ourselves to a three-dimensional flow $\vec{\phi}(t)=(X(t),\ Y(t),\ Z(t))$. Linearizing the flow about $\vec{\phi}(t)$, we obtain an equation for the evolution of the difference, denoted by $\delta\vec{\phi}$:

$$\delta\vec{\phi}=\frac{\partial F}{\partial\phi}|_{\phi(t)}\delta\vec{\phi},$$

where $\partial F/\partial\phi$ is a matrix which depends both on the flow and on the particular solution considered. Analytic integration of this equation is, except in special cases, impossible. However, it can always be integrated numerically, yielding a matrix $L(t)$ such that:

$$\delta\vec{\phi}(t)=L(t)\delta\vec{\phi}(0)$$

where $\delta\vec{\phi}(t)$ is the solution associated with an initial displacement $\delta\vec{\phi}(0)$. By virtue of the preceding relation, $L(0)=1$. The matrix $L$ is a square $m\times m$ matrix for a flow of dimension $m$, and has $m$ eigenvalues.

This is very similar to the Floquet theory for the linear stability of a periodic trajectory. The procedure has the same inspiration: linear analysis of the behavior in the vicinity of a trajectory. But whereas in the Floquet theory we only look at what happens after one period of a closed orbit, here this restriction is lifted. While the eigenvalues of the Floquet matrix give information about the linear stability of a limit cycle, the eigenvalues of $L$ give an information about the evolution near a trajectory not constrained to close upon itself.

Analytic integration is nevertheless easy when $\partial F/\partial\phi$ does not depend on time and its eigenvalues are the (possibly complex) numbers $\lambda_1$, $\lambda_2$ and $\lambda_3$. We arrive at a matrix $L(t)$ which is diagonal in the coordinate system of its eigenvectors:

$$L(t)=\begin{vmatrix}\Lambda_1 & 0 & 0\\ 0 & \Lambda_2 & 0\\ 0 & 0 & \Lambda_3\end{vmatrix}=\begin{vmatrix}e^{\lambda_1 t} & 0 & 0\\ 0 & e^{\lambda_2 t} & 0\\ 0 & 0 & e^{\lambda_3 t}\end{vmatrix}$$

Let us designate by $L^+$ the Hermitian conjugate matrix of $L$. The trace of $L^+L$ is equal to:

$$\mathrm{T_r}(L^+(t)L(t))=e^{(\lambda_1+\lambda_1^*)t}+e^{(\lambda_2+\lambda_2^*)t}+e^{(\lambda_3+\lambda_3^*)t}$$

When $t$ increases, the exponent with the largest real part, $\bar{\lambda}$, eventually dominates the other two terms, so that:

$$\bar{\lambda}=\lim_{t\to\infty}\frac{1}{2t}\ln[\mathrm{Tr}(L^+(t)L(t))].$$

Using this expression, we are able to find the largest real part, $\bar{\lambda}$ without having to use the usual methods for determination of eigenvalues. This is a non-negligible practical advantage, as $\bar{\lambda}$ dominates the behavior for long times. We therefore seek to extend it to more general situations.

Most of the times, the matrix $\partial F/\partial\phi$ depends on time and $L(t)$ cannot be put into the simple form above. There are two reasons for this: firstly, the eigenvalues of $\partial F/\partial\phi$ are not constant, and secondly, $L$ is not diagonalizable in a fixed reference frame. We can, however, still define the quantity:

$$\lambda_{[\phi]}=\lim_{t\to\infty}\frac{1}{2t}\ln[\mathrm{Tr}(L^{+}(t)L(t))]$$

because what are called multiplicative ergodic theorems establish the existence of this limit for a large category of situations. This limit is called the Lyapunov exponent (or Lyapunov number) associated with the solution $\vec{\phi}(t)$. It expresses the fact that, at long times, the difference $\delta\vec{\phi}$ grows or decays exponentially on the average, according to whether the sign of $\lambda_{[\phi]}$ is positive or negative.

In this study, we use the Fortran program given by Wolf et al. [10] in order to calculate the Lyapunov exponent.

### 2.4 Route to Chaos

What are the routes that lead a dynamical system from regular behavior to chaos? To answer this question, we must list the different possible transitions between attractors. The representative examples with appearance of chaos are quasi-periodicity, period-doubling bifurcation, and intermittency. [11, 12, 13, 14, 15]

In the first part, we emphasize the tendency of many dynamical systems to adopt periodic behavior, regardless of their other characteristics. Although periodicity does not exhaust the range of possibilities, a natural first step towards addressing the questions posed above is to examine the conditions under which a periodic regime loses its stability. To argue it, we give an account of floquet theory of linear stability of periodic solutions.

#### 2.4.1 Floquet's Theory

Consider a nonlinear autonomous flow in an $m$-dimensional phase space which has a periodic solution of period $T$:

$$\vec{X}(t+T)=\vec{X}(t).$$

To find out if this solution is stable or not, it suffices to look at what happens to a small initial displacement $\delta\vec{X}$ away from the solution. Linearizing the flow about the periodic trajectory, we find that an initial condition $\vec{X}_0+\delta\vec{X}$ ($\delta\vec{X}$ infinitesimal) is mapped at the end of the period $T$ into $\vec{X}_0+M\delta\vec{X}$, where $M$ is an $m\times m$ matrix called the Floquet matrix.

The problem of the linear stability of a periodic solution has been reduced in this way to the study of the eigenvalues of $M$. We first note that this matrix always has an eigenvalue equals to one : this corresponds to a displacement $\delta\vec{X}$ along the trajectory. The significance of this is simply that if we stay on the limit cycle, at the end of a period we arrive exactly at the point of departure : a trivial conclusion for a periodic solution, from which we learn nothing about its stability. Instead, we must study what happens in the directions perpendicular to the trajectory. We see intuitively that, while the eigenvalues of $M$ depend on the form of the limit cycle, they are independent of the reference point $\vec{X}_0$ chosen along it. Since over one period $\vec{X}_0+\delta\vec{X}$ is mapped into $\vec{X}_0+M\delta\vec{X}$, the solution is linearly stable if all of the eigenvalues of $M$ are located inside the unit circle $D$ of the complex plane. Then, all the components of the vector $\delta\vec{X}$ which are perpendicular to the limit cycle are reduced with each period. On the other hand if (at last) one of the eigenvalues of $M$ is outside of $D$, $\delta\vec{X}$ grows continually in at least one direction : the trajectory moves further and further away from the limit cycle, which is therefore unstable.

By continuous variation of a parameter $\mu$, the periodic solution gradually changes ; the same is true of the matrix $M$ and of its eigenvalues. Each of the eigenvalues can be represented in the complex plane by a curve parameterized by $\mu$. Loss of stability of the periodic solution, accompanied by a bifurcation, occurs when one of these curves exits from the inside of the unit circle to the outside as $\mu$ is varied. There exist the three possibilities for traversal of the unit circle $D$ by eigenvalues of the Floquet matrix : at (+1), at (−1) and at two complex conjugate eigenvalues($\alpha\pm i\beta$). Aside from the loss of stability, each of these crossing types, i. e. (+1), (−1) and ($\alpha\pm i\beta$), has different consequences on the later behavior of the system, which depend on the nonlinearities and are closely related to the bifurcations involved.

### 2.4.2 Bifurcation

When (+1) is crossed, a saddle-node bifurcation occurs. The periodic solution does not merely become unstable : it disappears entirely. In a parameter region slightly above the bifurcation threshold, the system enters a regime called the Type 1 intermittency. It is characterized by phases of regular, almost periodic behavior (laminar phases), interrupted from time to time by phases of apparently anarchical behavior (turbulent bursts).

If the circle is traversed at (−1), the bifurcation is called subharmonic, and may be either supercritical (normal) or subcritical (inverse). In the case of a supercritical subharmonic bifurcation, a new stable periodic solution, whose period is twice as long, replaces the solution which has become unstable. Period-doubling is repeated for each of the periodic solutions obtained, resulting in an infinite sequence of bifurcations called a subharmonic cascade and ending in chaos. A subcritical bifurcation, on the other hand, leads to the Type III intermittency, which qualitatively resembles the Type I intermittency : long phases of almost periodic behavior are interrupted from time to time by chaotic bursts. However, the Type III is characterized by progressive increase of the

Table 2. 1 Type of bifurcation.

| Crossing | Bifurcation | Phenomenon |
|---|---|---|
| $(+1)$ | Saddle-node | Type I intermittency |
| $(-1)$ | Subharmonic { normal | Subharmonic cascade |
| | Subharmonic { inverse | Type III intermittency |
| $(\alpha \pm i\beta)$ | Hopf { normal | Quasiperiodicity |
| | Hopf { inverse | Type II intermittency |

amplitude of the subharmonic during the almost periodic phase, the reason being that, here, nonlinear effects amplify the subharmonic instability of the limit cycle. The amplitude increases with each successive oscillation; when it exceeds a critical value, the laminar phase is interrupted.

Finally, a third mode of instability takes place when two complex conjugate eigenvalues $(\alpha \pm i\beta)$ simultaneously cross the unit circle: this is called a Hopf bifurcation. If the Hopf bifurcation is supercritical, it leads to a stable attractor, close to the limit cycle which is now unstable (but which still exists). This attractor is a torus $T^2$ on the surface of which is inscribed the new solution corresponding to a quasi-periodic regime. A second supercritical Hopf bifurcation can then generate a transition $T^2 \rightarrow T^3$ and the chaotic attractor appears as the outcome of a third bifurcation (possibly merged with the second). If the bifurcation is subcritical, we can encounter another phenomenon, called the Type II intermittency. The Type II intermittency has the same global qualitative features as the Type I and the Type III, except for the fact that the instabilities which develop during the laminar phases have a frequency which is unrelated to the ratio $\alpha/\beta$ where $(\alpha \pm i\beta)$ are the eigenvalues crossing the unit circle at the bifurcation. The dynamical process which indicates a new laminar phase after a turbulent burst is particularly complex to describe in this case, as it involves a flow in a six-dimensional phase space, which means a Poincaré section in $\boldsymbol{R}^5$. Table 2.1 summarizes the different situations we have described.

### 2.5 Theory of Intermittency

In this section, we analyze the intermittency in detail. According to Ref. [5], we briefly explain the theory of the intermittency. This theory is used to categorize the solutions with intermittency in the Lorenz and the five components models (Sec. 3.3).

We start from so called the Floquet matrix. Generically the eigenvalue of the Floquet matrix that crosses the unit circle $D$ (Sec. 2.4.1) has a unique eigenvector. This is the case for the Lorenz model. Let us then define a coordinate $u$ in the plane of the Poincaré section which points to the direction of the destabilizing eigenvector. (The Poincaré section is defined as a certain plane which is crossed trajectory in the phase space. We have placed the points of intersection corresponding to a given direction of the evolution of the trajectory such as $P_0$, $P_1$, $P_2$, $\cdots$ and so on. The transformation leading from one point to the next is as continuous mapping $T$ called the Poincare map, i. e., $P_{k+1}= T(P_k)=T^2(P_{k+1})=\cdots$) Using the eigenvalue $\Lambda(r)$ as the function of $r$, a new coordinate $u'$ by Poincaré mapping:

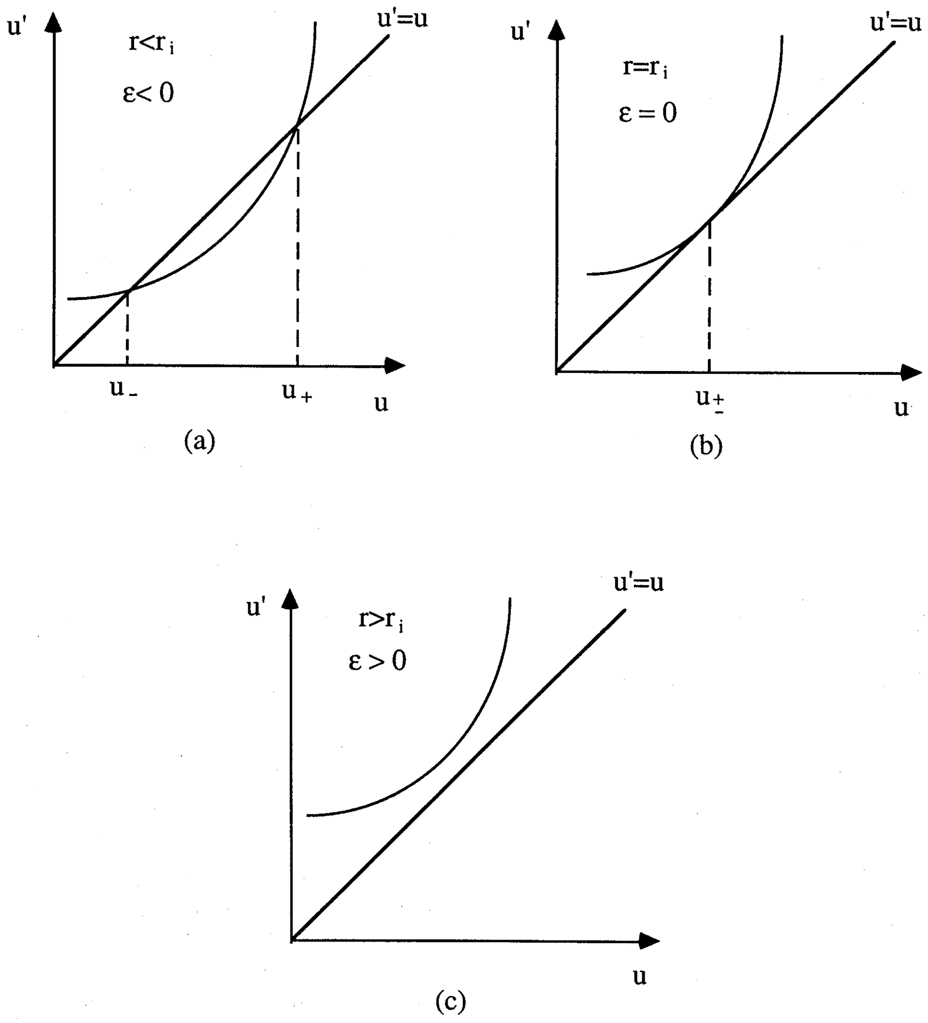


Fig. 2.1 Graph of $u|\rightarrow u'(u)$ near its fixed point.
(a) $u_+$ and $u_-$ are fixed points, so the trajectory is a limit cycle.
(b) $u'(u, r)$ is tangent to the identity map $u'=u$.
(c) A channel appears, therefore the intermittency occurs.

$$u' = \Lambda(r)u \tag{2.1}$$

At $r = r_i$ if the conditions $\Lambda(r_i) = 1$ and $(d\Lambda/dr)_{r_i} \neq 0$ are satisfied, we label that the crossing is $+1$. To have an idea what happens to the Poincaré mapping when $r$ varies near $r_i$, we will start from the approximation (to be justified further on) that Eq. (2.1) is expanded by the Taylor series of the function $u'(u, r)$ in the neighborhood of $u = 0$, and the origin is taken at $r = r_i$. We first take a few higher order terms into account.

A limit cycle for the dynamical system shows up as a fixed point of the Poincaré mapping. Near the fixed point for $r < r_i$, the curve of $u'(u)$ on $u' - u$ plane is almost tangent to the identity map ($u' = u$), since $(du'/du)_{r_i} = 1$ and $\Lambda(r_i) = 1$. We therefore find ourselves in the situation represented schematically in Figure 2.1(a). At the bifurcation point ($r = r_i$), the curve $u'(u)$ is exactly tangent to the identity map, since $(du'/du) = 1$ at the fixed point (Figure 2.1(b)). The passage from Fig. 2.1(a) to 2.1(b) is accomplished by translating the curve $u'(u)$ upwards. If $r$ continues to increase, the curve continues to move up, forming a small channel between itself and the identity map (Figure 2.1(c)).

The one-parameter family of curves near the contact point is represented by the following generic form for $u'$:

$$u' = u + \varepsilon + u^2 \tag{2.2}$$

The coefficient of $u^2$ (the second term of the Taylor series of $u'$ about $u = 0$ and $r = r_i$) has been taken to be unity by an appropriate choice of the scale for $u$. The parameter $\varepsilon$, proportional to $r - r_i$, is the control parameter which is varied to produce the transition from Fig. 2.1(a) to Fig. 2.1(c).

For $\varepsilon = 0$, we have the situation of Fig. 2.1(b): the equation $u'(u) = u$ has a double root at $u = 0$, with slope $(du'/du)_{u=0} = +1$. For $\varepsilon \neq 0$, fixed points of Eq. (2.2) are solutions of the equation $u'(u) = u$, i. e. $u_\pm = \pm(-\varepsilon)^{1/2}$, and exist only if $\varepsilon < 0$. Their Floquet eigenvalues are $(du'/du)_{u_\pm} = 1 \pm 2(-\varepsilon)^{1/2}$, so that the solution $u_-$ is stable, and $u_+$ is unstable. This is easily illustrated by using the graphical construction for iterating the transformation $u \to u'(u)$ (Figure 2.2).

The stable fixed point $u_-$ is an attractor for initial conditions $u < u_+$, and the fixed point $u_+$ is unstable. Iterations beginning from $u > u_+$ diverge rapidly like $(u^{(0)})^{2n}$, where $u^{(0)}$ is a value close to the initial value and $n$ is the number of iteration. Equation (2.2) represents the local change of $u$ near $r = r_i$, and indicates truncating the Taylor series of $u'(u, r)$ at the first order in $(r - r_i)$ and at the second order in $u$. This takes account of the fact that the slope $du'/du$ is close to unity near the considering bifurcation point.

We have seen that when $\varepsilon$ is small and positive, a narrow channel is created between the graphs of the identity map and of $u'(u)$. This has two important consequences:

i) First, for $\varepsilon > 0 (r \geq r_i)$ there no longer exists a fixed point of the first return map in the region considered.

ii) An iteration that starts from a negative value of $u$ will systematically drift towards the $u>0$ region (see Figure 2.3): because $\varepsilon$ and $u^2$ are positive, we have $u'=u+\varepsilon+u^2>u$.

But if $\varepsilon$ is very small, the successive iterations accumulate in the narrowest part of the channel. This brings us back to the question of intermittency. The region of the channel – more specifically, the $u$ values that we will actually observe – is very close to the fixed points that existed for $\varepsilon<0$. Therefore if we go back to the continuous time signal of the flow that corresponds to the passage through the channel for the Poincaré mapping, we find a time depen-

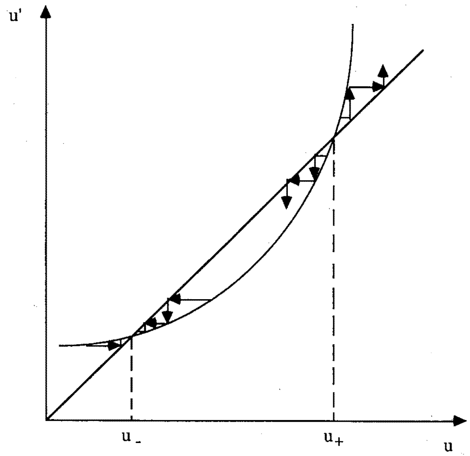


Fig. 2.2 Iteration of $u|\rightarrow u'(u)$ when two fixed points $u_\pm$ exist.

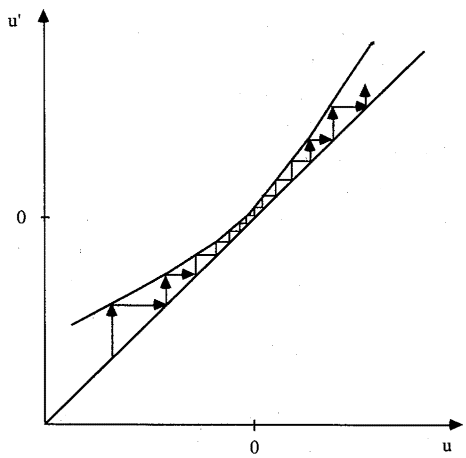


Fig. 2.3 Iteration of $u\rightarrow u'=u+\varepsilon+u^2$ for $\varepsilon>0$.

dence very similar to that of the stable oscillations taking place for $\varepsilon<0$. But the oscillations are no longer stable since the first return map $u \to u'(u, \varepsilon)$ no longer has a fixed point near 0, and so there is no periodic solution, stable or unstable, to the equations of motion near the limit cycle.

The Lorenz model exhibits an intermittent transition of the kind we have just described (in Sec. 3.3). Thus, we examine quantitative prediction of intermittency by the theory.

In a theoretical model, the physical parameters have been eliminated, leading to the universal form of the transformation $u \to u'(u)$:

$$u' = u + \varepsilon + u^2$$

a form which is valid in a neighborhood of $u=0$. The quantitative predictions deduced from this description will therefore be of the form of the *scaling laws* governing, for example, the average duration of laminar phases near $\varepsilon=0$. To find these laws, we notice that, if $u'$ is close to $u$, we can replace $u'-u$ by the derivative $du/dk$ ($k$ is the discrete time of iteration). We then replace the *difference* equation by the *differential* equation:

$$\frac{du}{dk} = \varepsilon + u^2 \tag{2.3}$$

This equation has as its general solution:

$$u(k) = \varepsilon^{1/2}\tan(\varepsilon^{1/2}(k-k_0)) \tag{2.4}$$

$k_0$ being approximately the step at which the iteration goes through the narrowest part of the channel. For simplicity we take $k_0=0$.

The function $u(k)$ diverges for $k=\pm(\pi/2)\varepsilon^{-1/2}$ (in fact for $k=(m\pi/2)\varepsilon^{-1/2}$, for any odd integer $m$). The meaning of this divergence is that when $k$ has attained the value of the order of $\varepsilon^{-1/2}$, $u'-u$, is no longer small, so that the difference equation (2.2) can no longer be replaced by the differential equation (2.3). This tells us that the number of iterations necessary to go through the channel is of order $\varepsilon^{-1/2}$, as does the interval of $k$ values between two consecutive divergences of Eq. (2.4). We have found a scaling law: the average duration of the laminar phases diverges like $\varepsilon^{-1/2} \sim |r-r_i|^{-1/2}$ as the threshold is approached.

When an intermittent transition occurs between the periodic and the turbulent regimes, the Lyapunov exponent $\lambda(\varepsilon)$ characterizing the level of instability of the turbulent trajectories is of the order of the inverse of the correlation time of the signal with itself. If we assume that the correlation disappears almost completely during the turbulent bursts, we deduce that the correlation time is of order $\varepsilon^{-1/2}$, like the mean time for channel traversal, and that its inverse, the Lyapunov exponent, obeys the law $\lambda(\varepsilon)_{\varepsilon\to 0+} \sim \varepsilon^{1/2}$. This law is indeed verified by the Lorenz model.

Another interesting quantity is the statistical distribution of the duration $\gamma$ of the laminar phases, that is $P(\tau, \varepsilon)$. In a sample of $N$ laminar phases ($N$

integer), there are $N \cdot \int_0^\tau d\tau' P(\tau', \varepsilon)$ phases which last less than $\tau$. We already know that the average duration of a laminar phase is $\int_0^\infty d\tau P(\tau, \varepsilon) \sim \varepsilon^{-1/2}$. For $\varepsilon$ fixed, the duration of a laminar phases is bounded from above by a quantity of order $\varepsilon^{-1/2}$, and the closer we get to the threshold, the less the duration fluctuates. These considerations allow us to draw a qualitative shape for $P(\gamma, \varepsilon)$ in an intermittent regime (Figure 2.4) of the laminar phases in the Type I.

The exact form of $P(\tau, \varepsilon)$ depends upon the details of the problem, as the fluctuations of $\tau$ reflect the fluctuations of the process of reinjection into the

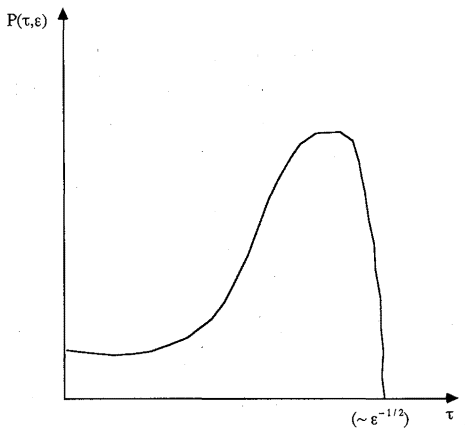


Fig. 2.4 Distribution of the length of laminar phases in the Type I intermittency.

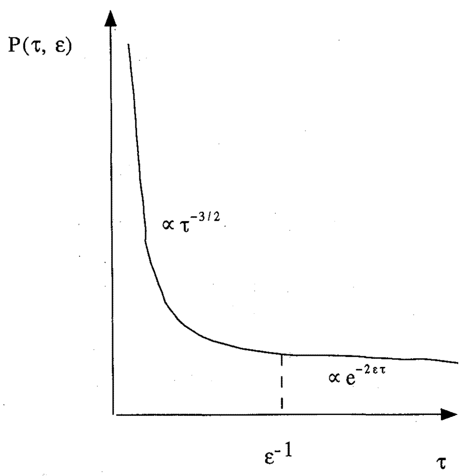


Fig. 2.5 Distribution of the length of laminar phases in the Type III intermittency.

channel. The distribution $P(\tau, \varepsilon)$ is more easily measured than the preceding scaling laws, which all require pinpointing the threshold $\varepsilon=0$ and thus a series of experiments at very closely spaced values of the control parameter. We note also that, for the other intermittency types (the Type II and III), the distribution of laminar phase duration follows a law very different from that of the Type I. These other distributions law have the maxima for short time scales and decrease algebraically in the large time scales.

Similarly, we can derive scaling law of the Type III intermittency. The result is following: $P(\tau)\sim\tau^{-3/2}$, for $1\ll\tau\ll\varepsilon^{-1}$, and $P(\tau)\sim exp(-2\varepsilon\tau)$, for $\tau\gg\varepsilon^{-1}$. The Lyapunov exponent is given by $\lambda(\varepsilon)\sim\varepsilon$. Distribution of the length of laminar phases in the Type III intermittency is shown in Figure 2.5.

## 2.6 Model Equation

Starting from one fluid MHD model, we derive RMHD model which is relevant to analyze the behavior of edge plasma with shear flow in the scrape-off layer (SOL) [16, 17, 19, 20]. The boundary condition appropriate to SOL is shown. The reduction of the freedom of RMHD model gives the modified Lorenz type model with five variables, i. e., the Lorenz type model with shear flow effect [16, 18, 19]. If the shear flow is turn off, this model reduces to the conventional Lorenz model with three variables. The analysis of the Lorenz model based on the numerical simulation is revisited.

### 2.6.1 One Fluid MHD Model

One Fluid MHD model which is our starting point is given as follows: equation of motion,

$$\rho\frac{d\mathbf{v}}{dt}=-\nabla p+\mathbf{j}\times\mathbf{B}+\mu\Delta\mathbf{v}, \tag{2.5}$$

continuity equation,

$$\frac{\partial\rho}{\partial t}+\nabla\cdot(\rho\mathbf{v})=0, \tag{2.6}$$

Ohm's law,

$$\mathbf{E}+\mathbf{v}\times\mathbf{B}=\eta\mathbf{j}, \tag{2.7}$$

adiabatic law of pressure,

$$\frac{d}{dt}(p\rho^{-\gamma})=0, \tag{2.8}$$

and Maxwell's equations,

$$\nabla\times\mathbf{E}=-\frac{\partial\mathbf{B}}{\partial t}, \tag{2.9}$$

$$\nabla\times\mathbf{B}=\mu_0\mathbf{j}, \tag{2.10}$$

$$\nabla\cdot\mathbf{B}=0, \tag{2.11}$$

where $\mu$, $\gamma$, and $\mu_0$ are the viscosity, the specific-heat ratio, and the magnetic permeability, respectively. Operator $\Delta$ denotes Laplacian.

### 2.6.2 Coordinates System

Now we consider coordinates system. Since we are interested in the behavior of SOL plasma in a toroidal system which is located at the region outside of separatrix, we treat the edge plasma region instead of the whole plasma region.

Figure 2.6 shows the schematic view of SOL in poloidal section. In this region, the magnetic field lines are connected to the divertor or the limiter so that they have the finite lengths. It is hold that the condition $L_c<\lambda$ in SOL, where $L_c$ is the characteristic length of field line called connection length and $\lambda$ is the typical mean free path of particles. This condition shows that the uniformity of plasma is kept along the field line. The direction of the magnetic field line is labeled by $z$. From the above condition, we have $\partial/\partial z=0$. The perpendicular surface to the magnetic field line is labeled by the coordinates ($x$, $y$), where $x$ corresponds to the radial direction of torus and $y$ corresponds to the poloidal direction of torus. We consider the situation that the effective gravity due to the magnetic field inhomogeneity acts on the $x$ direction and the plasma shear flow is in the $y$ direction. Two dimensional (2D) slab model is used to analyze this problem. For the boundary condition, we use the periodic boundary condition in the $y$ direction and we have the boundary $\pm d/2$ in the $x$ direction, where $x=-d/2$ corresponds to the separatrix and $d$ is the width of SOL.

### 2.6.3 RMHD Model

Here, the RMHD model equation is derived. On the assumption that the plasma is incompressible fluid, we have

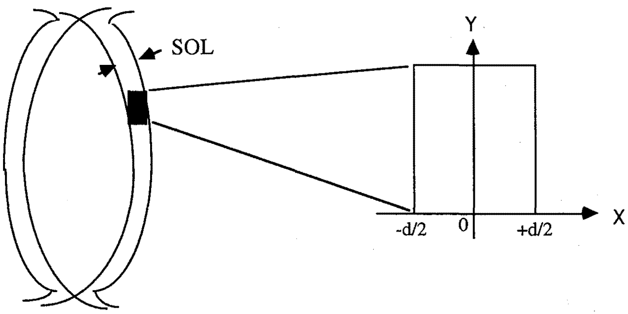


Fig. 2.6 The schematic view of SOL in poloidal section. Here we assume 2D slab plasma. Radial direction corresponds to the $x$ direction and poloidal direction corresponds to the $y$ direction in this model.

$$\nabla\cdot\mathbf{v}=0. \tag{2.12}$$

Then the continuity equation Eq. (2.6) is reduced to

$$\frac{\partial\rho}{\partial t}+\mathbf{v}\cdot\nabla\rho=0. \tag{2.13}$$

Combining Eq. (2.13) with Eq. (2.8), the adiabatic law of pressure is rewritten as

$$\frac{\partial p}{\partial t}+\mathbf{v}\cdot\nabla p=0. \tag{2.14}$$

This equation is valid when the fluid is non-dissipative and the change of the pressure is due to the convection. Introducing the effect of heat conduction, Eq. (2.14) is generalized as

$$\frac{\partial p}{\partial t}+\mathbf{v}\cdot\nabla p=\chi\Delta p, \tag{2.15}$$

where $\chi$ is the heat conductivity. This equation is used to describe the evolution of the pressure.

Next, we consider the equation of motion. Taking account of an effective gravity due to the curvature of the magnetic field line as an external force, Navier-Stokes equation gives rise to

$$\rho\frac{\partial\mathbf{v}}{\partial t}+\rho\mathbf{v}\cdot\nabla\mathbf{v}=-\nabla p+\rho G\hat{\mathbf{x}}+\mu\Delta\mathbf{v}, \tag{2.16}$$

where $\hat{\mathbf{x}}$ represents the unit vector of the $x$ direction, $G$ is an effective gravitational acceleration. To derive this equation, we assume no plasma current in the $z$ direction. The centrifugal force per unit volume is estimated as $\rho u^2/R$, where $R$ is the curvature radius of the magnetic field line and $\mathbf{u}$ is a guiding center velocity. Assuming that the typical velocity is estimated by that of the guiding center $u_T$, we have the relation $2p=\rho u^2{}_T$. Since the gravitational acceleration is balanced with the centrifugal force, it is followed that

$$\rho G=\frac{\rho u^2{}_T}{R}=\frac{2p}{R}, \tag{2.17}$$

showing that the gravitational acceleration $G$ depends on the plasma pressure $p$. Introducing a coefficient $g=2/(\rho R)$, Eq. (2.16) is written as

$$\rho\frac{\partial\mathbf{v}}{\partial t}+\rho\mathbf{v}\cdot\nabla\mathbf{v}=-\nabla p+\rho g p\hat{\mathbf{x}}+\mu\Delta\mathbf{v}. \tag{2.18}$$

Writing the variables as $p\to P_0+\tilde{p}$, $\mathbf{v}\to\mathbf{V}_0+\tilde{v}$, where the subscript 0 denotes the equilibrium quantity and $\sim$ stands for the fluctuating part, and using Boussinesq approximation, that is $\rho=\rho_0$, Eqs. (2.15) and (2.18) are splitted into the equations describing the equilibrium quantity and the fluctuating part, respectively. For the equilibrium quantity two following equations

$$\mathbf{V}_0\cdot\nabla\mathbf{V}_0=-\frac{\nabla P_0}{\rho_0}+P_0 g\hat{\mathbf{x}}+\nu\Delta\mathbf{V}_0 \tag{2.19}$$

and

$$\mathbf{V}_0 \cdot \nabla P_0 = \chi \Delta P_0 \tag{2.20}$$

are obtained. For the fluctuating part,

$$\frac{\partial \tilde{\mathbf{v}}}{\partial t} + \tilde{\mathbf{v}} \cdot \nabla \mathbf{V}_0 + \mathbf{V}_0 \cdot \nabla \tilde{\mathbf{v}} + \tilde{\mathbf{v}} \cdot \nabla \tilde{\mathbf{v}} = -\frac{\nabla \tilde{p}}{\rho_0} + pg\hat{x} + \nu \Delta \tilde{\mathbf{v}} \tag{2.21}$$

and

$$\frac{\partial \tilde{\mathbf{p}}}{\partial t} + \tilde{\mathbf{v}} \cdot \nabla \mathbf{P}_0 + \mathbf{V}_0 \cdot \nabla \tilde{\mathbf{p}} + \tilde{\mathbf{v}} \cdot \nabla \tilde{\mathbf{p}} = \chi \Delta \tilde{\mathbf{p}} \tag{2.22}$$

are obtained. Acting $\hat{z} \cdot \nabla \times$ to the equation of motion Eq. (2.21) and using the assumption of incompressibility Eq. (2.12), we obtain the vorticity equation,

$$\frac{\partial \omega}{\partial t} + \mathbf{v} \cdot \nabla \omega_0 + \mathbf{V}_0 \cdot \nabla \omega + \mathbf{v} \cdot \nabla \omega = -g\frac{\partial p}{\partial y} + \nu \Delta \omega, \tag{2.23}$$

where $\omega = \hat{\mathbf{z}} \cdot (\nabla \times \mathbf{v})$, and $\tilde{}$ is omitted for simplicity.

Fluid velocity of the plasma arises from the $\mathbf{E} \times \mathbf{B}$ drift motion. Introducing the electrostatic potential $\phi$, the fluid velocity of the plasma is written by $\mathbf{v} = \hat{\mathbf{z}} \times \nabla \phi$ in the electrostatic limit. Therefore the electrostatic potential is equivalent to a stream function. In this case, the vorticity is expressed as $\omega = \Delta_\perp \phi$, where $\Delta_\perp = \partial^2/\partial x^2 + \partial^2/\partial y^2$. Using two variables $\phi$ and $p$, Eqs. (2.23) and (2.22) are written as

$$\frac{\partial}{\partial t}\Delta_\perp \phi = -[\phi, \Delta_\perp \phi] - [\Phi_0, \Delta_\perp \phi] - [\phi, \Delta_\perp \Phi_0] - g\frac{\partial p}{\partial y} + \nu \Delta_\perp \Delta_\perp \phi \tag{2.24}$$

and

$$\frac{\partial}{\partial t} p = -[\phi, p] - [\Phi_0, p] - \kappa \frac{\partial \phi}{\partial y} + \chi \Delta_\perp p \tag{2.25}$$

where $P = P_0(x)$ is assumed, and $\kappa = -dP_0/dx$. The Poisson's bracket is defined by

$$[f, g] = \frac{\partial f}{\partial x}\frac{\partial g}{\partial y} - \frac{\partial f}{\partial y}\frac{\partial g}{\partial x}, \tag{2.26}$$

for any functions of $f$ and $g$.

The boundary condition are imposed as

$$p(x = \pm d/2) = 0, \tag{2.27}$$

for $p$ and

$$\phi(x = \pm d/2) = 0, \tag{2.28}$$

for stream function $\phi$. The slip-free boundary condition

$$\Delta_\perp \phi(x = \pm d/2) = 0 \tag{2.29}$$

is used for vorticity where the vorticity goes to zero at the boundaries of $x = \pm d/2$. The periodic boundary condition is adapted in the $y$ direction.

### 2.6.4 Lorenz Model

In the absence of the shear flow, Eqs. (2.24) and (2.25) are reduced to the equations of heat convection of the neutral fluid in the Boussinesq approximation. In this limit, the normalized equations are written as

$$\frac{\partial}{\partial t}\Delta_\perp\phi=-[\phi,\ \nabla_\perp\phi]+P_r\left(-\frac{\partial p}{\partial y}+\nabla_\perp\nabla_\perp\phi\right) \tag{2.30}$$

and

$$\frac{\partial}{\partial t}p=-[\phi,\ p]-R_a\frac{\partial\phi}{\partial y}+\nabla_\perp p, \tag{2.31}$$

where we use the normalization: $d$ for the scale of length, $d^2/\chi$ for the scale of time, $\chi$ for the scale of stream function, $\nu\chi/d^3g$ for the scale of pressure. Two dimensionless quantities, i. e., Rayleigh number $R_a$ and Prandtl number $P_r$ are introduced by

$$R_a=\frac{g\kappa d^4}{\nu\chi} \tag{2.32}$$

and

$$P_r=\frac{\nu}{\chi}. \tag{2.33}$$

Rayleigh number $R_a$ shows that a numerator corresponds to the magnitude of driving force of interchange instability [21] due to the gravity and the pressure gradient and a denominator corresponds to the magnitude of dissipation due to the heat conductivity and the viscosity. The larger the Rayleigh number is, the more the system unstable and turbulent becomes. On the other hand, the ratio of the viscosity to the heat conductivity, $P_r$, is related to the similarity of solutions. In the problem of thermal convection, it is known that the convective vortex called 'Bénard-cell' is created when the Rayleigh number exceeds a certain critical value and that the chaos is generated by this convection in the larger Rayleigh number regime. Equations (2.30) and (2.31) are the partial differential equations (PDE) and have infinite degrees of freedom.

A chaos in the heat convection problem is known to be generated even in the presence of the small degrees of freedom (a small numbers of the Fourier components). A set of the ordinary differential equations (ODE) called the 'Lorenz model', which consists of three Fourier components of the fields, has been utilized to analyze the chaotic behavior. Hereafter we shall revisit the Lorenz model. We start from Eqs. (2.30) and (2.31) with the boundary conditions Eqs. (2.27), (2.28), (2.29) and with the periodic boundary condition in the $y$-direction. Assuming that $\phi$ is described by only one Fourier component,

$$\phi(x,\ y,\ t)=\phi_1(t)\cos(\pi x)\sin(qy), \tag{2.34}$$

where $q=\frac{2\pi d}{L}$ indicated (normalized) wave number of cell (roll)-arrangement. Substituting Eq. (2.34) into Eq. (2.30) and Eq. (2.31), the equations

$$-\dot{\phi}_1(\pi^2+q^2)\cos(\pi x)\sin(qy)=-P_r\frac{\partial p}{\partial y}+P_r(\pi^2+q^2)^2\phi_1\cos(\pi x)\sin(qy)$$

and

$$\frac{\partial p}{\partial t}=\pi\phi_1\frac{\partial p}{\partial y}\sin(\pi x)\sin(qy)+q\frac{\partial p}{\partial x}\phi_1\cos(\pi x)\cos(qy)$$
$$-R_a q\phi_1\cos(\pi x)\cos(qy)+\Delta_\perp p$$

are obtained. Furthermore, we take the pressure perturbation in the form of

$$p(x,\ y,\ z)=p_1(t)\cos(\pi x)\cos(qy)+p_2(t)\sin(2\pi x), \tag{2.35}$$

where the term $\sin(2\pi x)$ is added in the pressure field which corresponds to the higher harmonic component of Fourier mode generated by the convective nonlinearity.

Substituting Eq. (2.34) and Eq. (2.35) into Eq. (2.30) and Eq. (2.31), we obtain the dynamic equations for $\phi_1$, $p_1$ and $p_2$ as

$$\dot{\phi}_1=-\frac{P_r q}{\pi^2+q^2}p_1-P_r(\pi^2+q^2)\phi_1, \tag{2.36}$$

$$\dot{p}_1=\pi q\phi_1 p_2-R_a q\phi_1-(\pi^2+q^2)p_1, \tag{2.37}$$

and

$$\dot{p}_2=-\frac{1}{2}\pi\phi_1 p_1-4\pi^2 p_2. \tag{2.38}$$

Using the normalization and introducing variables $X$, $Y$ and $Z$, which represent $\phi_1$, $p_1$ and $p_2$ respectively, as

$$\tau=(\pi^2+q^2)t, \tag{2.39}$$

$$X=-\frac{\pi q}{\sqrt{2}(\pi^2+q^2)}\phi_1, \tag{2.40}$$

$$Y=\frac{\pi q^2}{\sqrt{2}(\pi^2+q^2)^3}p_1, \tag{2.41}$$

and

$$Z=\frac{\pi q^2}{(\pi^2+q^2)^3}p_2, \tag{2.42}$$

the Lorenz model is written as follows:

$$\frac{dX}{d\tau}=P_r(Y-X), \tag{2.43}$$

$$\frac{dY}{d\tau}=-XZ+rX-Y, \tag{2.44}$$

and

$$\frac{dZ}{d\tau}=XY-bZ, \tag{2.45}$$

with

$$r=\frac{q^2}{(\pi^2+q^2)^3}R_a \tag{2.46}$$

and

$$b=\frac{4\pi^2}{\pi^2+q^2}. \tag{2.47}$$

Let us discuss the stability analysis of the stationary solutions of the Lorenz model. The analysis is done for the fixed points of the model equations. The fixed points are obtained by letting $\partial/\partial\tau=0$ in Eqs. (2.43), (2.44) and (2.45), as (0, 0, 0) and $(\pm\sqrt{b(r-1)},\ \pm\sqrt{b(r-1)},\ r-1)$. We categorize a parameter regime into three according to the value of normalized Rayleigh number $r$, i. e., (1) $0<r<1$, (2) $1<r<r_c$ and (3) $r>r_c$, where $r_c=P_r(P_r+b+3)/(P_r-b-1)$.

In the regime (1), $0<r<1$, only the fixed point

$$(0,\ 0,\ 0) \tag{2.48}$$

is stable.

In the regime (2), $1<r<r_c$, the fixed points

$$(\pm\sqrt{b(r-1)},\ \pm\sqrt{b(r-1)},\ r-1) \tag{2.49}$$

are stable but the fixed point (0, 0, 0) is unstable.

In the regime (3), $r>r_c$, all the fixed point are unstable.

In order to explain the behavior of Bénard convection described by the Lorenz model, we show the results from the numerical simulation. The parameters are given by $P_r=10.0$, $b=8/3$ and $r_c=24.74$.

For the parameter regime (1), $0<r<1$, the solution converges to (0, 0, 0) for any initial values. There is not convection in this parameter regime, where the heat is transmitted from the bottom to the top. The temperature difference between the top and the bottom remains small.

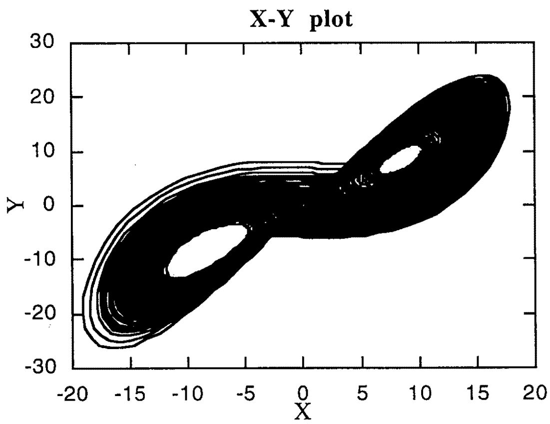


Fig. 2.7 Trajectory in the phase space projected on the $X$-$Y$ plane. In the 3D space, the trajectory like the plumage of a butterfly corresponds to a chaotic attractor or a strange attractor.

In the parameter regime (2), $1<r<r_c$, the stable fixed points are given by $(\sqrt{\frac{8}{3}(r-1)}, \sqrt{\frac{8}{3}(r-1)}, r-1)$ and $(-\sqrt{\frac{8}{3}(r-1)}, -\sqrt{\frac{8}{3}(r-1)}, r-1)$. The convection is generated in this regime. The temperature difference becomes rather larger than that in the regime (1).

In the regime (3) $r>r_c$, three fixed points are unstable and the chaotic behavior of the solution in the phase space is observed.

Figure 2.7 shows a chaotic attractor in the case with $r=28$. The trajectory

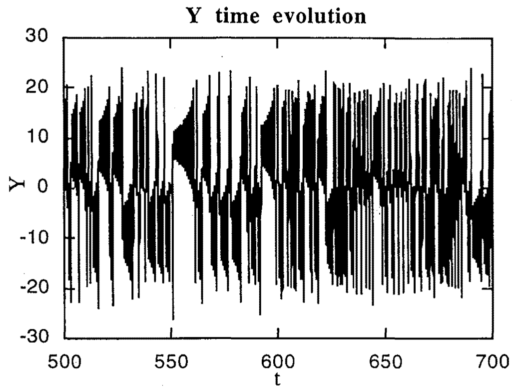


(a)

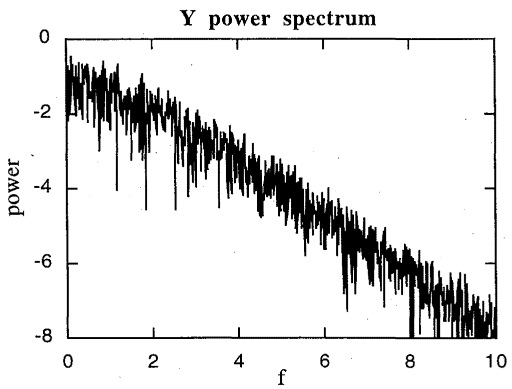


(b)

Fig. 2.8 (a) the time evolution of $Y$ showing the non-periodic oscillation,
(b) the power spectrum of $Y$ which is the continuous spectrum.

in the phase space is projected on $X-Y$ plane. The chaotic attractor shows that the trajectory goes around the fixed points $(6\sqrt{2}, 6\sqrt{2}, 27)$ and $(-6\sqrt{2}, -6\sqrt{2}, 27)$, and that the structure consists of many sheets but a thin sheet or a thick sheet.

Figure 2.8(a) shows the time evolution of $Y$ and (b) shows the power spectrum of $Y$ respectively, those correspond to the case shown in Fig. 2.7. These plots show the typical nature of a chaos, i. e., the irregularity and complexity of the temporal behavior of the solution, having the continuous and broadband spectrum. Convection is broken down and the turbulence appears in this regime.

For the case with the larger value of $r$, a limit cycle, a period-doubling bifurcation, an intermittent transition and a chaotic attractor are observed. Finally a stable limit cycle re-appears for the extremely large value of $r$.

Figure 2.9 shows the three components of the Lyapunov exponent versus the normalized Rayleigh number $r$. The positive value of the maximum Lyapunov exponent corresponds to the appearance of chaos and when the exponent is zero the periodic oscillation is observed.

The intermittent transition to a chaos is observed in the Lorenz model. To examine this transition, numerical simulation is performed changing $r$ for the fixed parameters of $P_r=10.0$ and $b=\frac{8}{3}$. The intermittency appears near $r=$

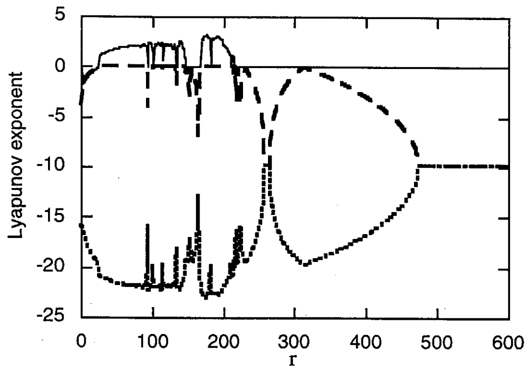


Fig. 2.9 The relation between the Lyapunov exponent and $r$. When the maximum exponent is positive, the system is chaotic, and zero exponent corresponds to the periodic oscillation. At $r=28$, the maximum exponent is positive, which corresponds to the appearance of chaos. Near $r=166$ the exponent changes from zero to the positive value, where intermittent transition to chaos is observed.

(a)

(b)

(c)

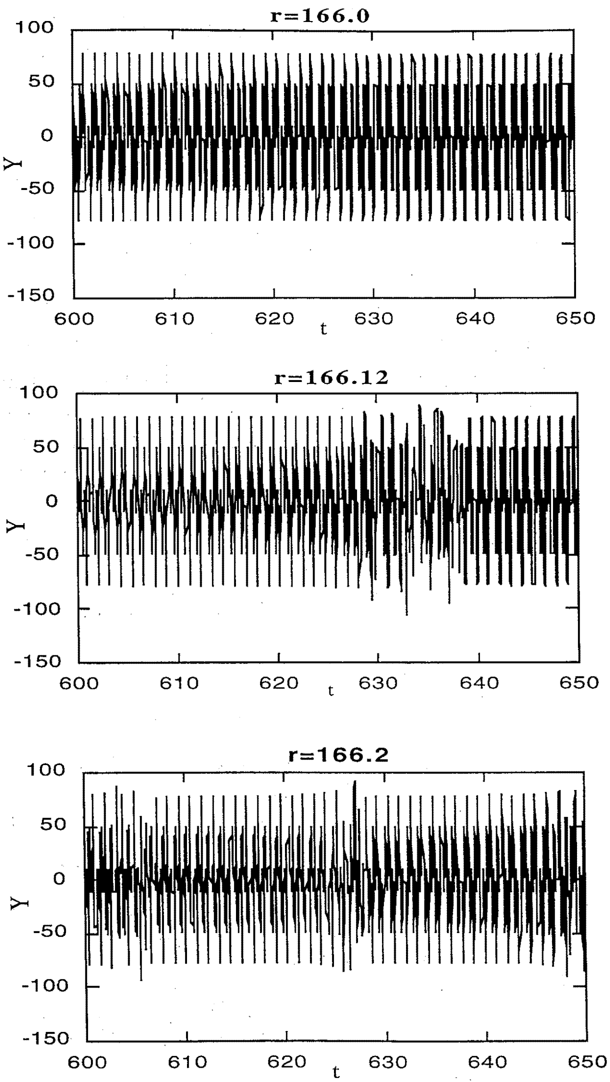


Fig. 2.10 The appearance of the intermittent regime of the Lorenz model is shown calculating the cases for (a) $r=166.0$, (b) $r=166.12$, and (c) $r=166.2$. Time evolution of $Y$ is illustrated. In this parameter regime, the intermittency appears at $r_i=166.07$. When $r<r_i$, the periodic oscillation is observed as is shown by (a). For the larger values of $r$, (b) (c), the burst appears more frequently.

166.

Figure 2.10 shows the time evolution of $Y$ in the cases with $r=166.0$, $r=166.12$, and $r=166.2$. In Fig. 2.10(b) the burst exists at a place near $t=629\sim637$, while in (c) the bursts occur at three places near $t=603\sim605$, $t=626\sim628$ and $t=648$. A qualitative definition of the burst is that it occurs suddenly with the short time duration of the increase of amplitude. Our quantitative definition will be presented in Sec. 3.2. The larger the value of $r$ is, the more frequent the burst is. It is known that this intermittency corresponds to the Type I.

## § 3. Comparison of Three and Five Components Models

Three components model has been studied extensively as is seen in Chapter 2. In this chapter, we present a five components model [18] and we perform the numerical simulation of the model. The simulation results of the three components model are compared with those of the five components model based on the Lyapunov analysis, which is a novel point in this thesis.

### 3.1 Derivation of Five Components Model

The Lorenz model derived in Chap. 2 does not include the shear flow in the $y$ direction. The Lorenz model has been extended [18, 19] by introducing the new Fourier harmonics which represent the shear flow. According to the following procedure, we derive the model equation.

We start from Eqs. (2.30) and (2.31) with Eqs. (2.34) and (2.35), and the same boundary conditions as in the Lorenz model are used here, i. e., Eqs. (2.27), (2.28), and (2.29) in the $x$ direction, and periodic condition in the $y$ direction. Assuming that $\phi$ is still described by a small number of the Fourier modes, we add new Fourier harmonics into $\phi$ field as

$$\phi(x, y, t)=\phi_1(t)\cos(\pi x)\sin(qy) + \phi_2(t)\cos(\pi x)+\phi_3(t)\sin(2\pi x)\cos(qy). \tag{3.1}$$

Two terms are added to Eq. (2.34), i. e., the term which is proportional to cos $(\pi x)$ contains the shear flow in the y-direction and the term proportional to sin $(2\pi x)\cos(qy)$ corresponds to the higher harmonics generated by the nonlinear coupling between the introduced shear flow and the pressure perturbation $p$. As for $p$, we use the same equation Eq. (2.35) as the Lorenz model.

In order to visualize the convection patterns of $\phi(x, y)$ and $p(x, y)$, we show the basic patterns of Fourier components in $x-y$ plane which appear in basic equations, Eqs. (3.1) and (2.35). In Figure 3.1, the basic convection patterns of $\phi(x, y)$ are illustrated: (a) the fundamental component $\phi_1\cos(\pi x)\sin(qy)$ (Bēnard cell type), (b) the shear flow component $\phi_2\cos(\pi x)$, (c) the higher harmonic one $\phi_3\sin(2\pi x)\cos(qy)$ and (d) the combination of all the components with the same weightings. Here we choose $\phi_1=\phi_2=\phi_3=1$ and $q=\pi$. The white color corresponds to the positive value and the black color to the negative value. According to the change of color from black to white, the value changes its sign from minus to plus. In Figure 3.2, the convection patterns of the pressure are shown: (a) the fundamental component $p_1\cos(\pi x)\cos(qy)$, (b) the quasi-linear term $p_2\sin(2\pi x)$ and (c) their combination for $p_1=p_2=1$ and $q=\pi$. The convection pattern can be deformed by the shear flow component from Fig. 3.1(a) to Fig. 3.1(d).

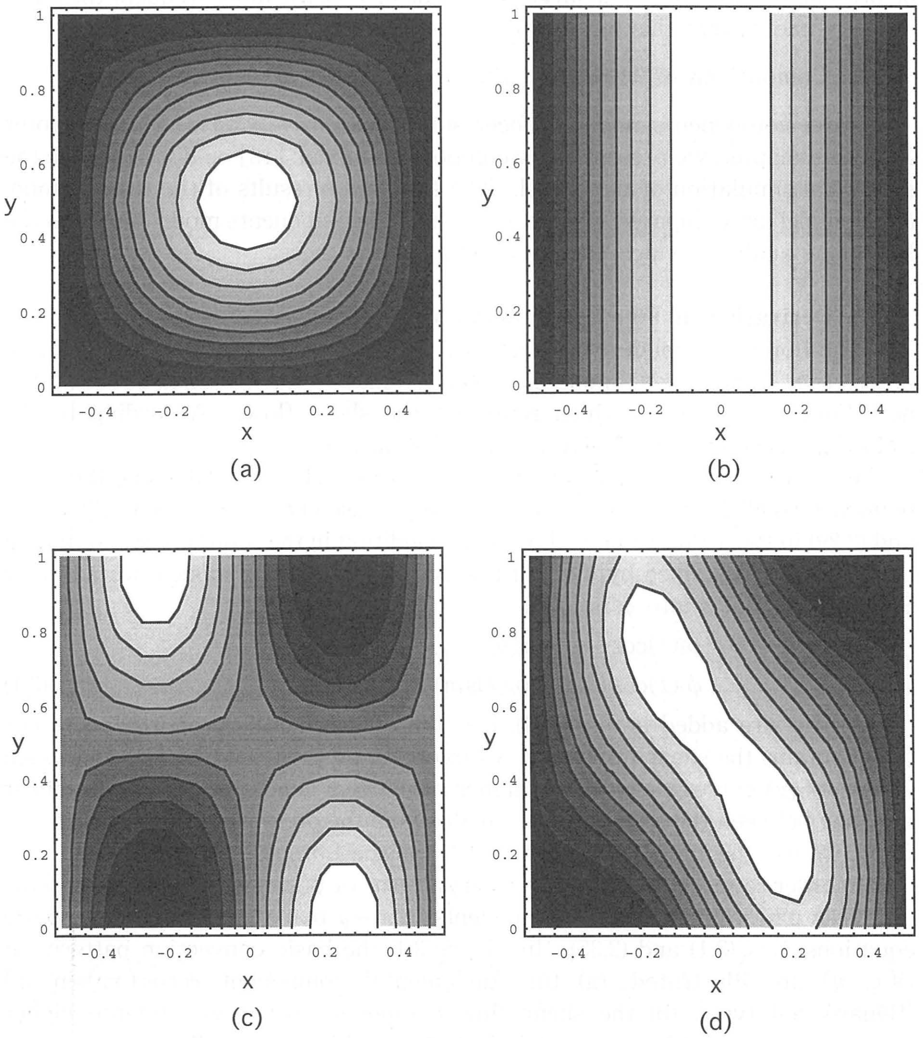


Fig. 3.1 (a) $\phi_1\cos(\pi x)\sin(qy)$, (b) $\phi_2\cos(\pi x)$, (c) $\phi_3\sin(2\pi x)\cos(qy)$, (d) (a)+(b)+(c), where $\phi_1=\phi_2=\phi_3=1$ and $q=\pi$. A horizontal axis indicates the $x$ direction and a vertical axis does the $y$ direction. The boundary of $x$ is $-0.5$ and $0.5$ and the $y$ direction is periodic.

Substituting Eqs. (3.1) and (2.35) into Eq. (2.30),

$$-\dot{\phi}_1(\pi^2+q^2)\cos(\pi x)\sin(qy)-\dot{\phi}_2\pi^2\cos(\pi x)$$
$$-\dot{\phi}_3(4\pi^2+q^2)\sin(2\pi x)\cos(qy)$$
$$=-\frac{\pi}{2}q^3\phi_1\phi_2\sin(2\pi x)\cos(qy)$$

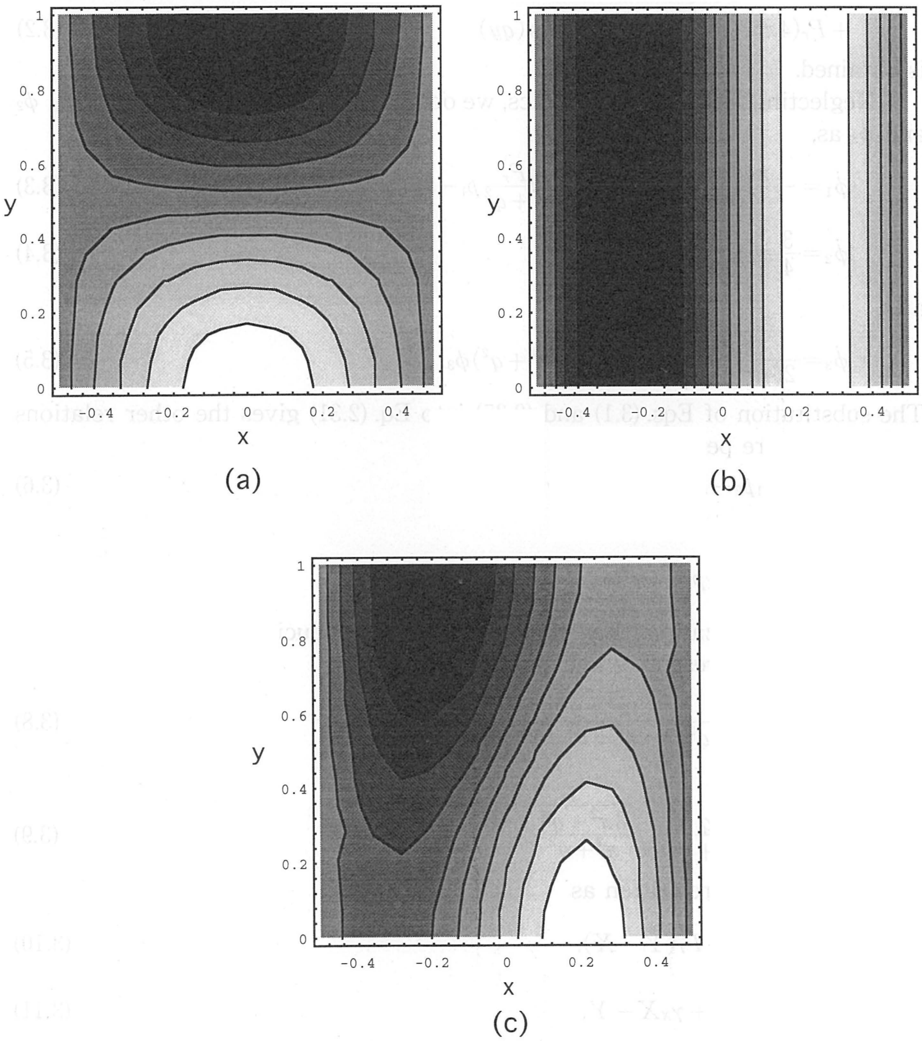


Fig. 3.2 (a) $p_1\cos(\pi x)\cos(qy)$, (b) $p_2\sin(2\pi)$, (c) (a)+(b), where $p_1=p_2=1$ and $q=\pi$. A horizontal axis indicates $x$ direction and a vertical axis does the $y$ direction. The boundary of $x$ is $-0.5$ and 0.5 and the $y$ direction is periodic.

$$+\frac{3}{4}\pi^3\phi_1\phi_3\{\cos(\pi x)-\cos(3\pi x)\}\{1-\cos(2qy)\}$$

$$-\frac{3}{2}\pi^3\phi_1\phi_3\{\cos(\pi x)+\cos(3\pi x)\}\{1+\cos(2qy)\}$$

$$+\frac{\pi}{2}q(3\pi^2+q^2)\phi_2\phi_3\{\cos(\pi x)-\sin(3\pi x)\}\sin(qy)$$

$$+P_r(\pi^2+q^2)^2\phi_1\{\cos(\pi x)\sin(qy)+P_r\pi^4\phi_2\cos(\pi x)$$

$$+P_r(4\pi^2+q^2)^2\phi_3\sin(2\pi x)\cos(qy) \tag{3.2}$$

is obtained.

Neglecting the higher harmonics, we obtain the dynamic equations for $\phi_1$, $\phi_2$ and $\phi_3$ as,

$$\dot{\phi}_1=-\frac{\pi q(3\pi^2+q^2)}{2(\pi^2+q^2)}\phi_2\phi_3-\frac{qP_r}{\pi^2+q^2}p_1-P_r(\pi^2+q^2)\phi_1, \tag{3.3}$$

$$\dot{\phi}_2=\frac{3}{4}\pi q\phi_1\phi_3-P_r\pi^2\phi_2, \tag{3.4}$$

and

$$\dot{\phi}_3=\frac{\pi q^3}{2(4\pi^2+q^2)}\phi_1\phi_2-P_r(4\pi^2+q^2)\phi_3. \tag{3.5}$$

The substitution of Eqs. (3.1) and (2.35) into Eq. (2.31) gives the other relations for the pressure perturbation, $p_1$ and $p_2$, as

$$\dot{p}_1=\pi q\phi_1 p_2-R_a q\phi_1-(\pi^2+q^2)p_1 \tag{3.6}$$

and

$$\dot{p}_2=-\frac{1}{2}\pi q\phi_1 p_1-4\pi^2 p_2. \tag{3.7}$$

Using the normalization: Eqs. (2.39)-(2.42) and introducing new variables of $V$ and $W$, which represent $\phi_2$ and $\phi_3$ respectively, as

$$V=\frac{\pi q}{\sqrt{3}(\pi^2+q^2)}\sqrt{\frac{3\pi^2+q^2}{\pi^2+q^2}}\phi_2, \tag{3.8}$$

and

$$W=\frac{\sqrt{3}\pi q}{2\sqrt{2}(\pi^2+q^2)}\sqrt{\frac{3\pi^2+q^2}{\pi^2+q^2}}\phi_3, \tag{3.9}$$

Eqs. (3.3)-(3.7) are rewritten as

$$\frac{dX}{d\tau}=VW+P_r(Y-X), \tag{3.10}$$

$$\frac{dY}{d\tau}=-XZ+\gamma_X X-Y, \tag{3.11}$$

$$\frac{dZ}{d\tau}=XY-\gamma_Z Z, \tag{3.12}$$

$$\frac{dV}{d\tau}=-XW-\gamma_V V, \tag{3.13}$$

and

$$\frac{dW}{d\tau}=-CXV-\gamma_W W. \tag{3.14}$$

Here non-dimensional parameters are introduced as

$$\gamma_X=\frac{q^2}{(\pi^2+q^2)^3}R_a, \tag{3.15}$$

$$\gamma_Z=\frac{4\pi^2}{\pi^2+q^2}, \tag{3.16}$$

$$\gamma_V=\frac{\pi^2}{\pi^2+q^2}P_r, \tag{3.17}$$

$$\gamma_W=\frac{4\pi^2+q^2}{\pi^2+q^2}P_r, \tag{3.18}$$

and

$$C=\frac{3q^2}{4(4\pi^2+q^2)}. \tag{3.19}$$

Equations (3.10)-(3.14) constitute the five components equations of the extended Lorenz model [18, 19].

The stability analysis around the fixed point, i. e., stationary solution of (X, Y, Z, V, W) has been done in Ref. [19] and the results are shown below. The fixed points are given by setting $(\dot{X}, \dot{Y}, \dot{Z}, \dot{V}, \dot{W})=(0, 0, 0, 0, 0)$. The number of the fixed points are seven and they are found to be (0, 0, 0, 0, 0), $(\pm\sqrt{\gamma_Z(\gamma_X-1)}, \pm\sqrt{\gamma_Z(\gamma_X-1)}, \gamma_X-1, 0, 0)$, $\left(\pm\sqrt{\frac{\gamma_V\gamma_W}{C}}, \pm\frac{\sqrt{C\gamma_V\gamma_W}\gamma_X\gamma_Z}{\gamma_V\gamma_W+\gamma_Z C}, \frac{\gamma_X\gamma_V\gamma_W}{\gamma_V\gamma_W+\gamma_Z C}, \pm\sqrt{-\frac{P_r\gamma_W}{C}\frac{\gamma_V\gamma_W+\gamma_Z C(1-\gamma_X)}{\gamma_V\gamma_W+\gamma_Z C}}, -\sqrt{-P_r\gamma_V\frac{\gamma_V\gamma_W+\gamma_Z C(1-\gamma_X)}{\gamma_V\gamma_W+\gamma_Z C}}\right)$ and $\left(\pm\sqrt{\frac{\gamma_V\gamma_W}{C}}, \pm\frac{\sqrt{C\gamma_V\gamma_W}\gamma_X\gamma_Z}{\gamma_V\gamma_W+\gamma_Z C}, \frac{\gamma_X\gamma_V\gamma_W}{\gamma_V\gamma_W+\gamma_Z C}, \mp\sqrt{-\frac{P_r\gamma_W}{C}\frac{\gamma_V\gamma_W+\gamma_Z C(1-\gamma_X)}{\gamma_V\gamma_W+\gamma_Z C}}, \sqrt{-P_r\gamma_V\frac{\gamma_V\gamma_W+\gamma_Z C(1-\gamma_X)}{\gamma_V\gamma_W+\gamma_Z C}}\right)$.

Three regimes for fixed points are identified according to the value of $\gamma_X$ (normalized Rayleigh number). They are (1) $0<\gamma_X<1$, (2) $1<\gamma_X<\gamma_{t1}$ and (3) $\gamma_{t1}<\gamma_X$, where $\gamma_{t1}\equiv 1+\frac{\gamma_V\gamma_W}{\gamma_Z C}$.

In the regime (1), $0<\gamma_X<1$, one fixed point,

$$(0, 0, 0, 0, 0) \tag{3.20}$$

appears and is stable. But it becomes unstable for $\gamma_X>1$.

In the regime (2), $1<\gamma_X<\gamma_{t1}$, two fixed points,

$$(\pm\sqrt{\gamma_Z(\gamma_X-1)}, \pm\sqrt{\gamma_Z(\gamma_X-1)}, \gamma_X-1, 0, 0) \tag{3.21}$$

appear. The bifurcation of the solution occurs at $\gamma_X=1$.

In the regime (3), $\gamma_{t1}<\gamma_X$, four fixed points

$$\left(\pm\sqrt{\frac{\gamma_V\gamma_W}{c}},\ \pm\frac{\sqrt{c\gamma_V\gamma_W}\gamma_X\gamma_Z}{\gamma_V\gamma_W+\gamma_Z c},\ \frac{\gamma_X\gamma_V\gamma_W}{\gamma_V\gamma_W+\gamma_Z c},\right.$$
$$\left.\pm\sqrt{-\frac{P_r\gamma_W}{c}\frac{\gamma_V\gamma_W+\gamma_Z c(1-\gamma_X)}{\gamma_V\gamma_W+\gamma_Z c}},\ -\sqrt{-P_r\gamma_V\frac{\gamma_V\gamma_W+\gamma_Z c(1-\gamma_X)}{\gamma_V\gamma_W+\gamma_Z c}}\right) \tag{3.22}$$

and

$$\left(\pm\sqrt{\frac{\gamma_V\gamma_W}{c}},\ \pm\frac{\sqrt{c\gamma_V\gamma_W}\gamma_X\gamma_Z}{\gamma_V\gamma_W+\gamma_Z c},\ \frac{\gamma_X\gamma_V\gamma_W}{\gamma_V\gamma_W+\gamma_Z c},\right.$$
$$\left.\mp\sqrt{-\frac{P_r\gamma_W}{c}\frac{\gamma_V\gamma_W+\gamma_Z c(1-\gamma_X)}{\gamma_V\gamma_W+\gamma_Z c}},\ \sqrt{-P_r\gamma_V\frac{\gamma_V\gamma_W+\gamma_Z c(1-\gamma_X)}{\gamma_V\gamma_W+\gamma_Z c}}\right) \tag{3.23}$$

appear. The bifurcation of the solution occurs at $\gamma_X=\gamma_{t1}$.

For the stability in the regime (2) and (3), two limits are considered. The first case is $1<\gamma_{t2}<\gamma_{t1}$, where $\gamma_{t2}\equiv\dfrac{P_r(\gamma_Z+P_r+3)}{P_r-1-\gamma_Z}$. Equation (3.21) becomes unstable for $\gamma_X>\gamma_{t2}$ and Eqs. (3.22)-(3.23) become unstable for $\gamma_X>\gamma_{t1}$.

The second case is $\gamma_{t2}<1$ $(P_r<\gamma_Z+1)$ or $\gamma_{t1}<\gamma_{t2}$. Equation (3.21) becomes unstable for $\gamma_X>\gamma_{t1}$. In the case $\gamma_{t2}<1$, Eqs. (3.22)-(3.23) become unstable for $\gamma_X>\gamma_{t3}>\gamma_{t1}$, where $\gamma_{t3}$ is some critical value.

When all stationary solutions become unstable, the limit cycles and the chaotic attractor appear.

### 3.2 Numerical Analyses

Numerical simulations of the three components model (Lorenz model) (2.43)-(2.45) and the five components model (3.10)-(3.14) are carried out and their results are shown below.

In these simulations, the normalized Rayleigh number

$$r=\gamma_X=\frac{R_a}{8\pi^4} \tag{3.24}$$

is chosen to be an order parameter to characterize the system behavior and the other parameters are fixed as

$$b=\gamma_Z=2.0,\ \gamma_V=2.0,\ \gamma_W=10.0,\ c=0.15,\ q=\pi,\ P_r=4.0.$$

When these parameters are chosen as above values, the critical values and the stationary solutions become as follows.

For the three components model:

(1) $0<r<1$

$(0,\ 0,\ 0)$

(2) $1<r<36$

$(\pm\sqrt{2(r-1)},\ \pm\sqrt{2(r-1)},\ r-1)$

(3) $r>36$ All the stationary solutions are unstable.

For the five components model:

(1) $0<\gamma_X<1$

$(0,\ 0,\ 0,\ 0,\ 0)$

(2) $1<\gamma_X<\frac{203}{3}(\gamma_{t1}=\frac{203}{3},\ \gamma_{t2}=36)$

$(\pm\sqrt{2(\gamma_X-1)},\ \pm\sqrt{2(\gamma_X-1)},\ \gamma_X-1,\ 0,\ 0)$

(3) $\frac{203}{3}<\gamma_X$

$$\left(\pm\frac{20\sqrt{10}}{3},\ \pm\frac{2\sqrt{3}\gamma_X}{20.3},\ \frac{20\gamma_X}{20.3},\ \pm\sqrt{-\frac{800}{3}\frac{20.3-0.3\gamma_X}{20.3}},\ -\sqrt{-8\frac{20.3-0.3\gamma_X}{20.3}}\right)$$

and

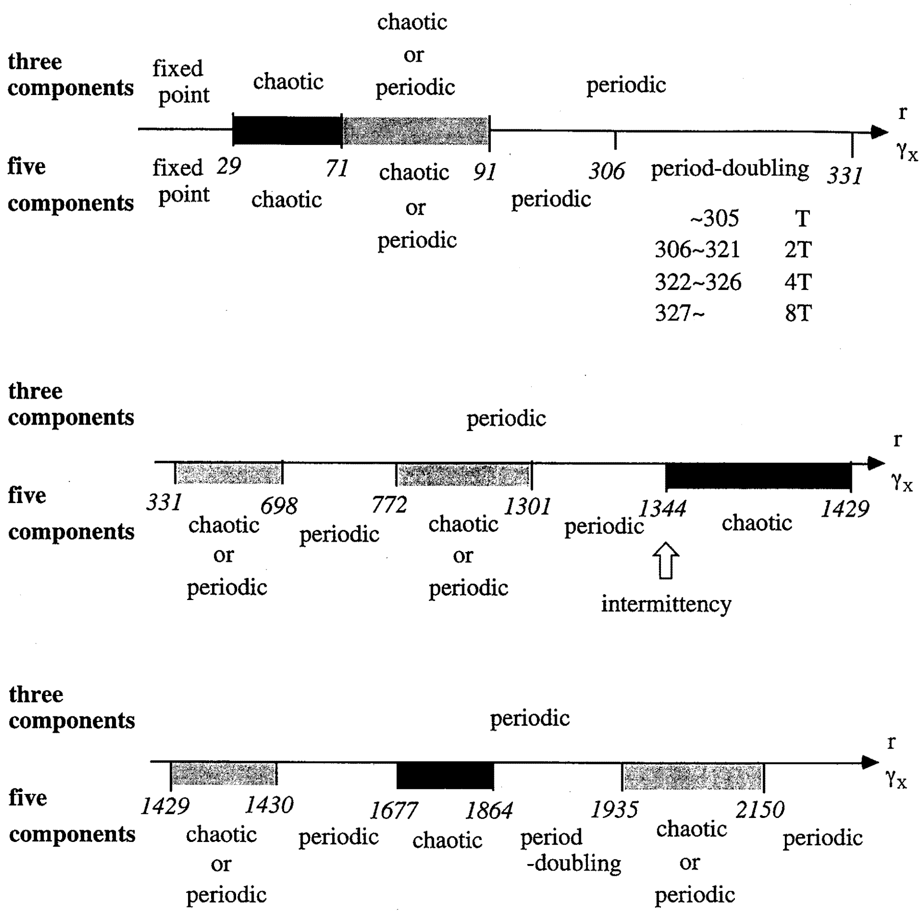


Fig. 3.3 Comparison beween successive change of attractors for three components system and for five components system for $P_r=4.0$. Controll parameter is $r$ and $\gamma_X$.

$$\left(\pm\frac{20\sqrt{10}}{3},\ \pm\frac{2\sqrt{3}\gamma_X}{20.3},\ \frac{20\gamma_X}{20.3},\ \mp\sqrt{-\frac{800}{3}\frac{20.3-0.3\gamma_X}{20.3}},\ -\sqrt{-8\frac{20.3-0.3\gamma_X}{20.3}}\right)$$

Initial values are given in the three components models as

$(X,\ Y,\ Z)=(1.0,\ 1.0,\ 1.0)$

and those in the five components model are

$(X,\ Y,\ Z,\ V,\ W)=(1.0,\ 1.0,\ 1.0,\ 1.0,\ 1.0).$

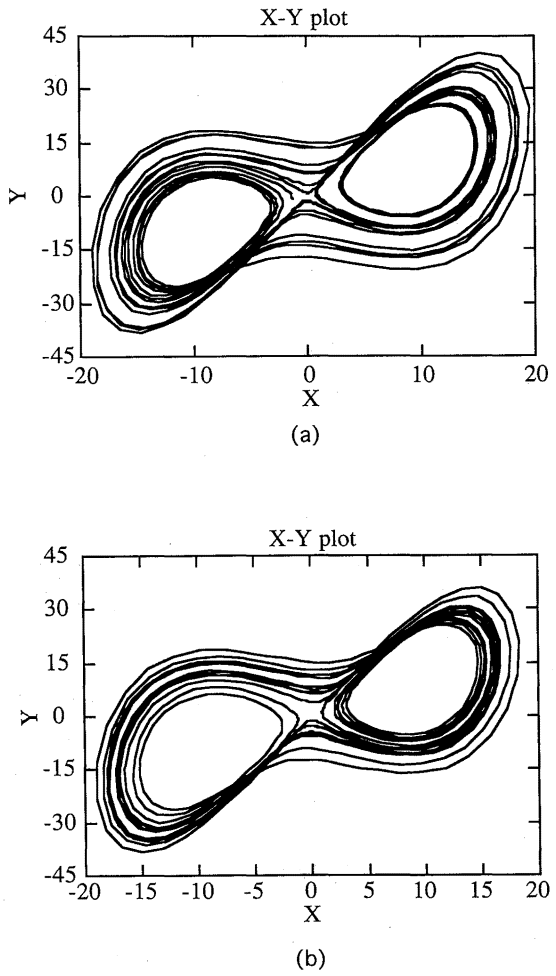


Fig. 3.4 Trajectory in phase space is projected to $X-Y$ plane at $r=\gamma_X=50.0$. (a) the three components model (b) the five components model

Three components model has been extensively investigated for the parameters $P_r=10.0$ and $b=8/3$ [2, 22] (Sec. 2.6.4). Here we choose the parameters as $P_r=4.0$ and $b=\gamma_Z=2.0$ to compare both models based on the Lyapunov analysis. Figure 3.3 shows the comparison between successive change of attractors for the three and the five components models with respect to the control parameter $r$ or $\gamma_X$. This figure is drawn based on the maximum Lyapunov exponent shown in Fiugre 3.14, which will be explained in the latter half of this section. Typical examples of the trajectory in the phase space, the time evolution of $Y$ and the power spectrum of $Y$ for specific values of $r$ or $\gamma_X$ are shown. The variables

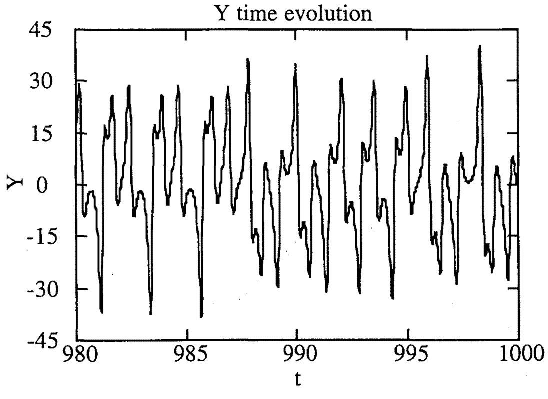


(a)

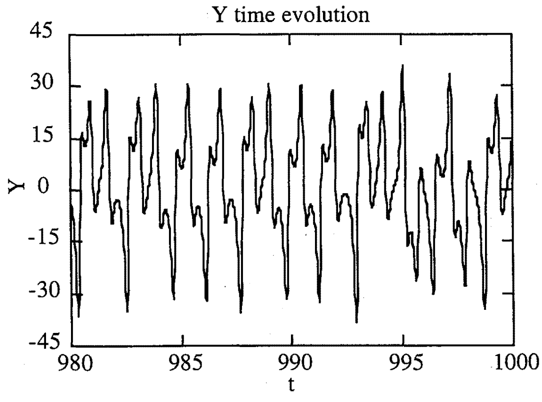


(b)

Fig. 3.5 Time evolution of $Y$ is shown at $r=\gamma_X=50.0$.
(a) the three components model
(b) the five components model

$X$, $Y$, $Z$, $V$ and $W$ correspond to the fields $\phi_1$, $p_1$, $p_2$, $\phi_2$ and $\phi_3$ respectively.

Case (1) $r = \gamma_X = 50.0$

At this value, both the three components model and the five components model give the chaotic solutions. The chaotic behavior is seen in Figures 3.4–3.6. Figure 3.4 compares the three components model (a) and the five components model (b), showing the trajectories of the solutions in the phase space projected on $X - Y$ plane. Initial trajectory traced from the initial value to the

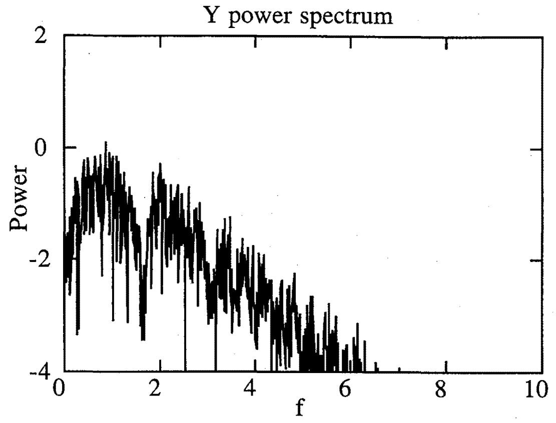


(a)

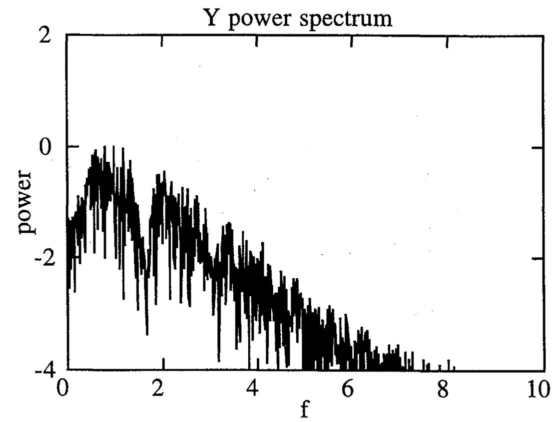


(b)

Fig. 3.6 Power spectrum of $Y$ is shown at $r = \gamma_X = 50.0$.
(a) the three components model
(b) the five components model

attractors is omitted for simplicity. Both trajectories in (a) and (b) are the chaotic attractors. Temporal evolutions of $Y$ are shown in Fig. 3.5(a) and (b), indicating the irregular oscillations. According to the change of the sign of $Y$, the sign of the pressure perturbation $p_1$ shown in Fig. 3.2(a) changes. The associated power spectra of $Y$ are shown in Fig. 3.6(a) and (b). The continuous

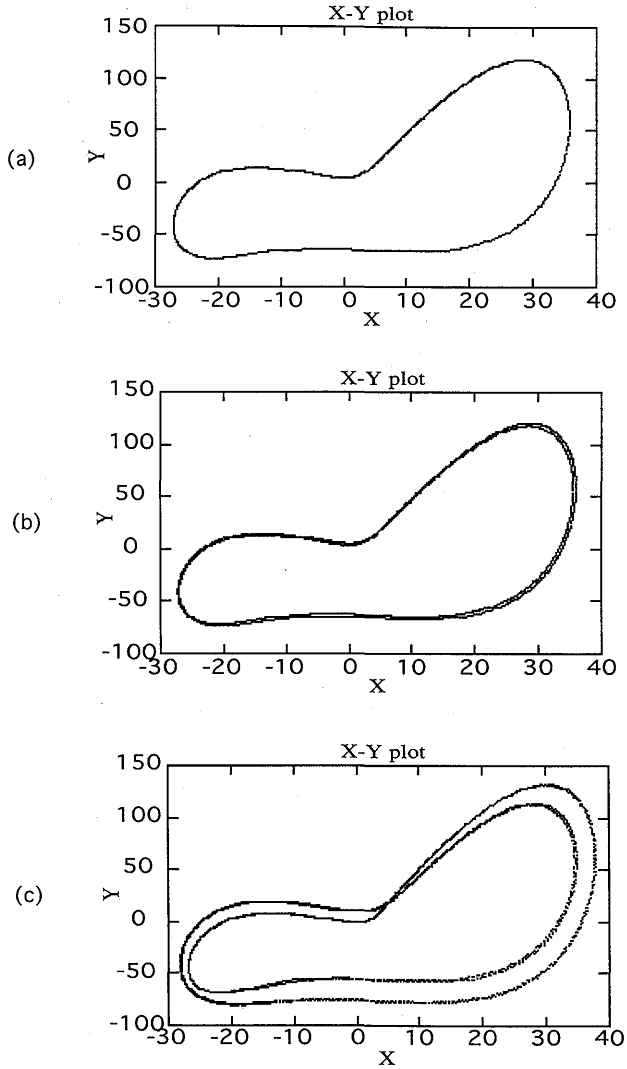


Fig. 3.7 The period-doubling process is shown in trajectory in the $(X, Y)$ phase space. (a) $\gamma =_{\mathrm{x}}= 305.0$ basic period. (b) $\gamma_{\mathrm{x}}=306.0$ twice period. (c) $\gamma_{\mathrm{x}}=322.0$ four times period.

spectrum which is the typical characteristics of chaos is observed in each case.

Case (2) $\gamma_X \cong 305$

Near this value, the period-doubling bifurcation is found to occur in the five components model, while only the periodic solution is found in the three components model.

Figure 3.7 shows the trajectories of the phase space for the five components model in cases with (a) $\gamma_X=305$, (b) $\gamma_X=306$, and (c) $\gamma_X=322$, respectively. At $\gamma_X$

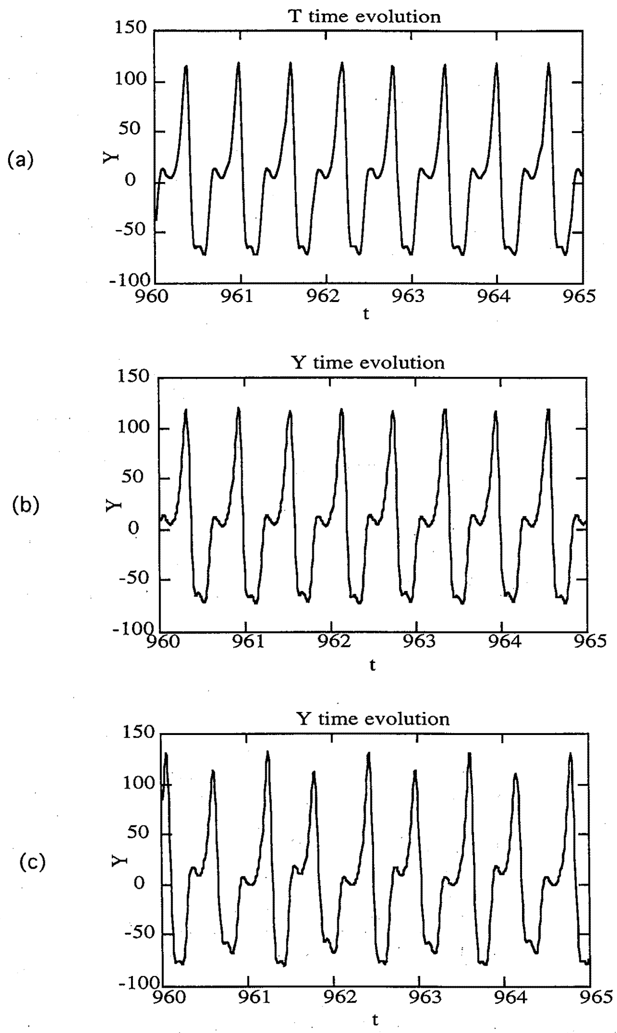


Fig. 3.8 The time evolution of $Y$ associated with the period-doubling is shown, for the cases of (a), (b), and (c) in Fig. 3.7.

$=305$, the first limit cycle solution appears, and the second limit cycle of the twice period is seen at $\gamma_X=306$. At $\gamma_X=322$, the third limit cycle of the period of four times is found. The successive period-doubling occurs as $\gamma_X$ increases. Associated time evolution of $Y$ for each case is shown in Figure 3.8. The period of each case is roughly estimated to be (a) 0.6, (b) 1.2, and (c) 2.4. In order to show the period-doubling process the power spectrum for each case is measured and is shown in Figure 3.9, where (a) shows the basic frequencies and their fine peaks are observed, (b) the basic frequencies and the half of them are seen, and

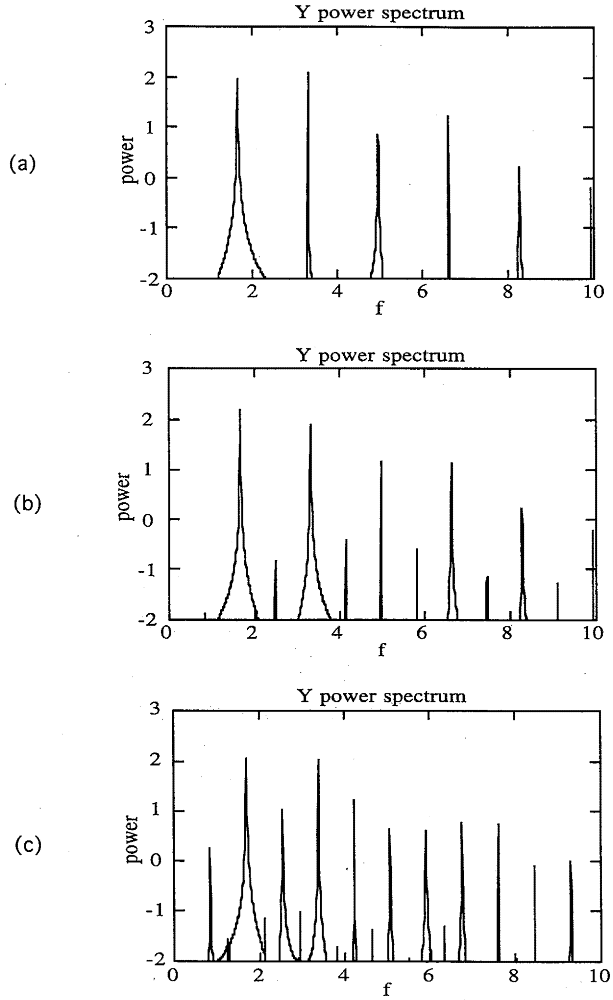


Fig. 3.9 The power spectrum of $Y$ corresponding to the case of (a), (b), and (c) in Fig. 3.7 are shown.

(c) further one-fourth of the basic frequencies are seen. The frequency which is eight times smaller than the basic frequency, exists but is difficult to be recognized in the plots. After the successive period-doubling of infinite times, the system becomes chaotic. This is understood as a typical example of a route to a chaos from the period-doubling bifurcation.

Case (3) $r=\gamma_X=400.0$

When $r$ and $\gamma_X$ become a few hundreds, it is found that there appears the considerable difference between the three components model and the five components model as seen from Fig. 3.3. Let us show the difference in the case

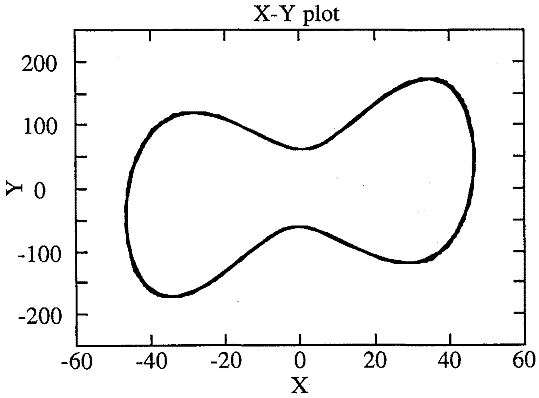


(a)

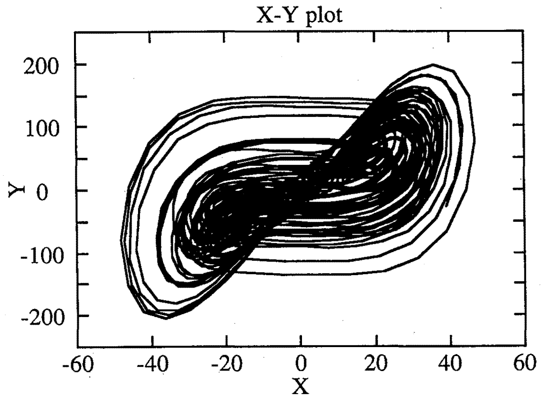


(b)

Fig. 3.10 Projected trajectory in phase space at $r=\gamma_X=400.0$.
(a) the three components model.
(b) the five components model.

of $r=\gamma_X=400.0$. The trajectory of the phase space $(X,\ Y)$ is compared in Figure 3.10 where the three components model shows the limit cycle solution (a), on the other hand the five components model shows the chaotic attractor (b). Figure 3.11 depicts the time evolution of $Y$ corresponding to the cases in Fig. 3. 10. It is shown that in the three components model the solution is the periodic oscillation, while in the five components model the irregular oscillation is found. The power spectrum corresponding to the cases in Fig. 3.10 is shown in Fig. 3. 12. Peaks of the basic frequencies are observed in the three components model, on the other hand the continuous spectrum is seen in the five components model.

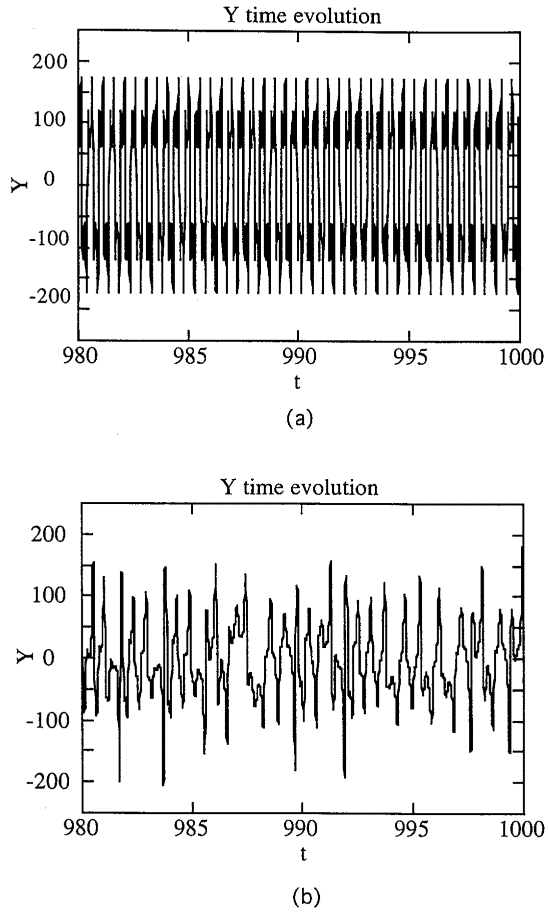


Fig. 3.11 Time evolution of $Y$ at $r=\gamma_x=400.0$.
(a) the three components model
(b) the five components model

Case (4) $\gamma_X \cong 1345$

An intermittent transition is found to take place in the five components model, while only the periodic solution is found for the three components model near this value.

The time evolution of $Y$ in the cases with (a) $\gamma_X=1345.16$, (b) $\gamma_X=1345.17$, (c) $\gamma_X=1345.19$, and (d) $\gamma_X=1345.30$ are depicted in Figure 3.13 to show the appearance of the intermittent behavior. The intermittency threshold is calculated to be $\gamma_{X_t}=1345.16784$ by surveying the value at which the Lyapunov exponent becomes closest to zero. Bellow this threshold, the periodic oscillation

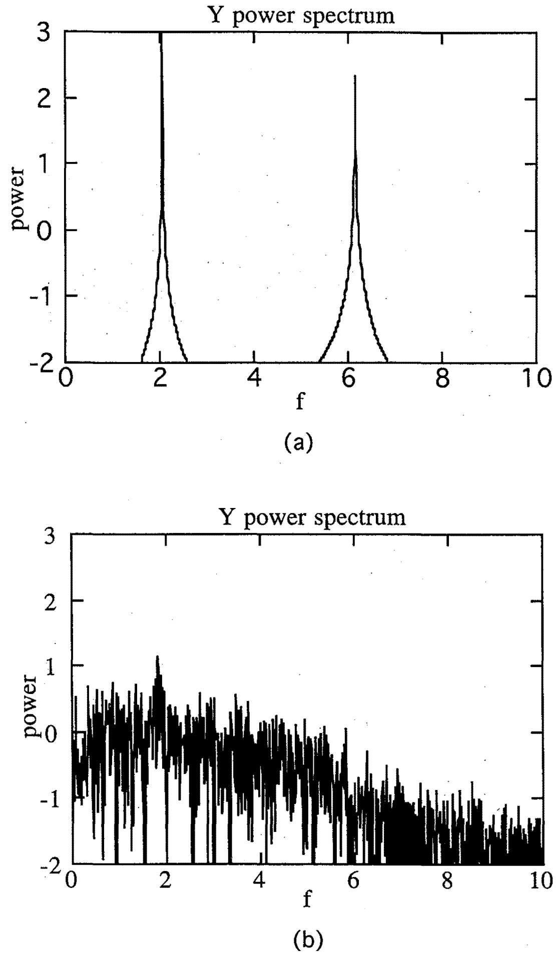


Fig. 3.12 Power spectrum of $Y$ at $r=\gamma_X=400.0$.
(a) the three components model
(b) the five components model

is observed as is shown in Fig. 3.13(a). When the value of $\gamma_X$ exceeds $\gamma_{Xi}$, bursts in the amplitude $Y$ appear (Fig. 3.13(b)). In Fig. 3.13(b) the bursts exist two places near $t=540\sim560$ and $t=870\sim880$. We here quantitatively define the burst when we observe an increase in 10% of the amplitude beyond its average maximum value. The larger $\gamma_X$ is, the more bursts appear (Fig. 3.13(c)). In Fig. 3.13(c) the bursts occur four places near $t=570\sim590$, $t=690\sim710$, $t=810\sim820$ and $t=930\sim950$. The chaotic behavior is seen in Fig. 3.13(d). This intermittency will be studied in detail in the next section.

Above typical cases are depicted from the parameter survey of $r$ and $\gamma_X$ which is shown in Fig. 3.3. In order to understand these transitions, we calculate

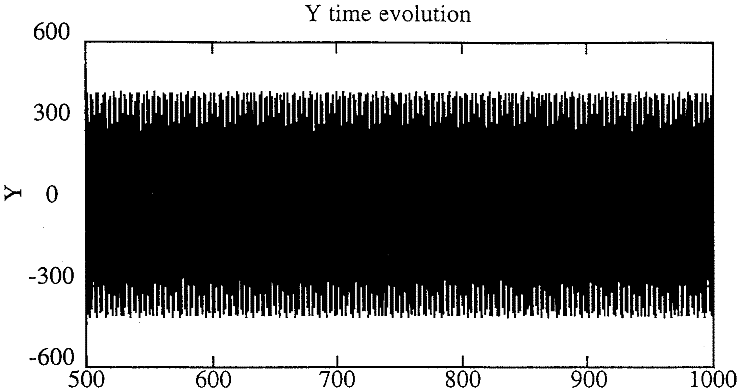


(a)

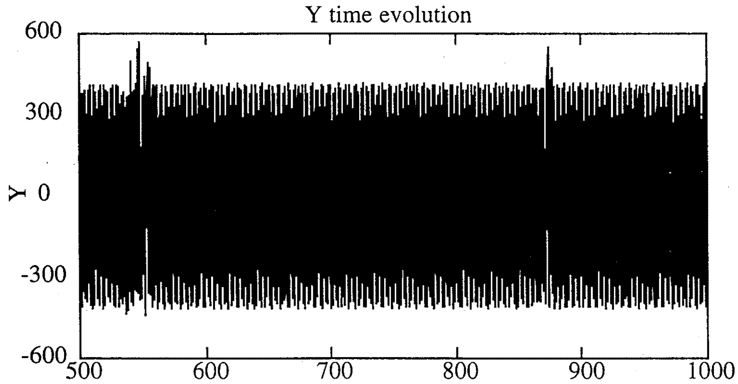


(b)

Fig. 3.13 Time evolution of $Y$ for the five components model
(a) at $\gamma_X=1345.16$
(b) at $\gamma_X=1345.17$

the Lyapunov exponents for the three components model and for the five components model. Parameters $r$ and $\gamma_X$ are surveyed from zero upto 4000. As is discussed in the previous chapter, if the maximum Lyapunov exponent exists to be positive, then the system becomes chaotic. The periodic solution is found if the maximum exponent is zero. If we only find the negative value of the exponent, the solution converges to the fixed points.

Nothing these facts, we show the Lyapunov exponents versus $r$ and $\gamma_X$ (normalized Rayleigh number) in the case with $P_r=4.0$ in Fig. 3.14. The exponents for the three components model and for the five components model are shown in (a) and (b), respectively. In the three components model, 1) the regime

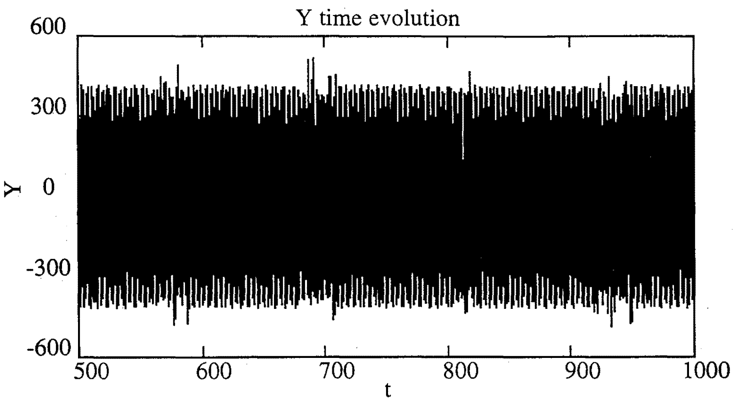


(c)

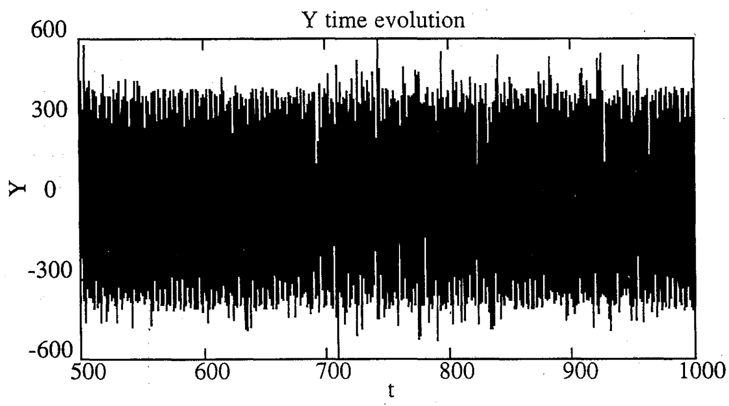


(d)

Fig. 3.13 Time evolution of $Y$ for the five components model
(c) at $\gamma_X=1345.19$
(d) at $\gamma_X=1345.30$

$0<r<29$ has the fixed point, 2) the regime $29<r<71$ has the chaotic solution with the positive value of the maximum Lyapunov exponent, 3) the regime $71<r<91$ has either the positive value or zero of the maximum exponent, and 4) the regime of $91<r$ has only the periodic solution (i. e. the maximum exponent is

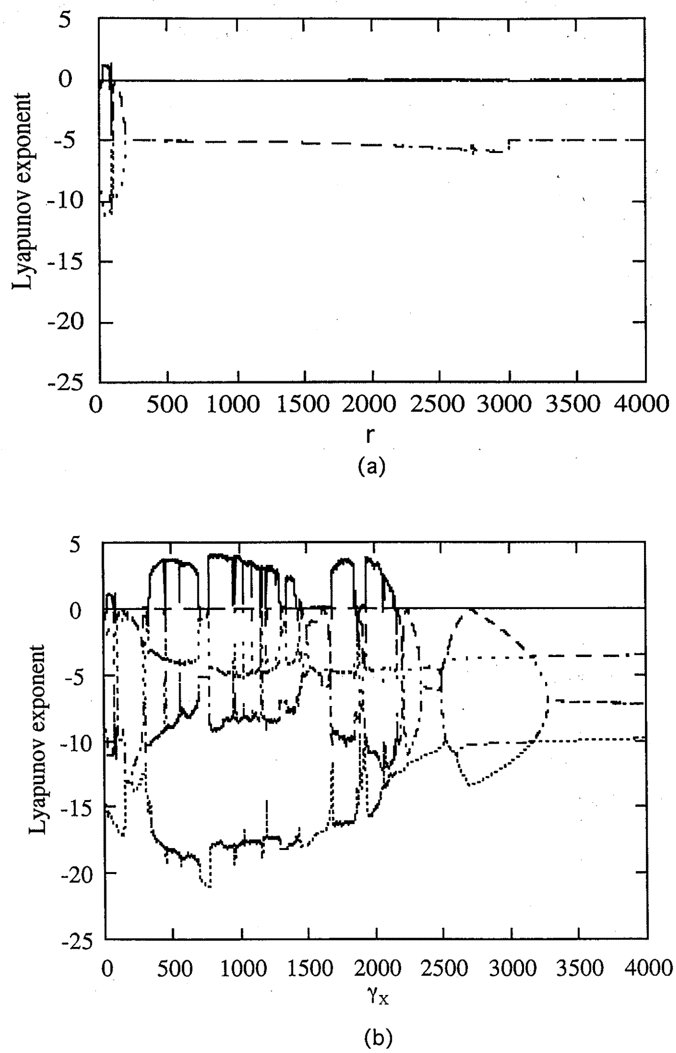


Fig. 3.14 The relation between the Lyapunov exponent and $r$ or $\gamma_x$ for $P_r=4.0$. One of the exponent is on the zero line in (a) and (b).
(a) the three components model
(b) the five components model

zero) which falls into the limit cycle. The analysis by use of the Lyapunov exponent is illustrated in the upper level of the lines shown in Fig. 3.3.

Concerning the five components model, the similar behavior of the Lyapunov exponent is observed to that of the three components model for the parameter regime of $r=\gamma_X<140$. As seen in Fig. 3.14(b), the positive value of the maximum Lyapunov exponent appears and disappears in the regime of $306<\gamma_X<2200$. We observe the chaotic behavior and the limit cycle solution as well

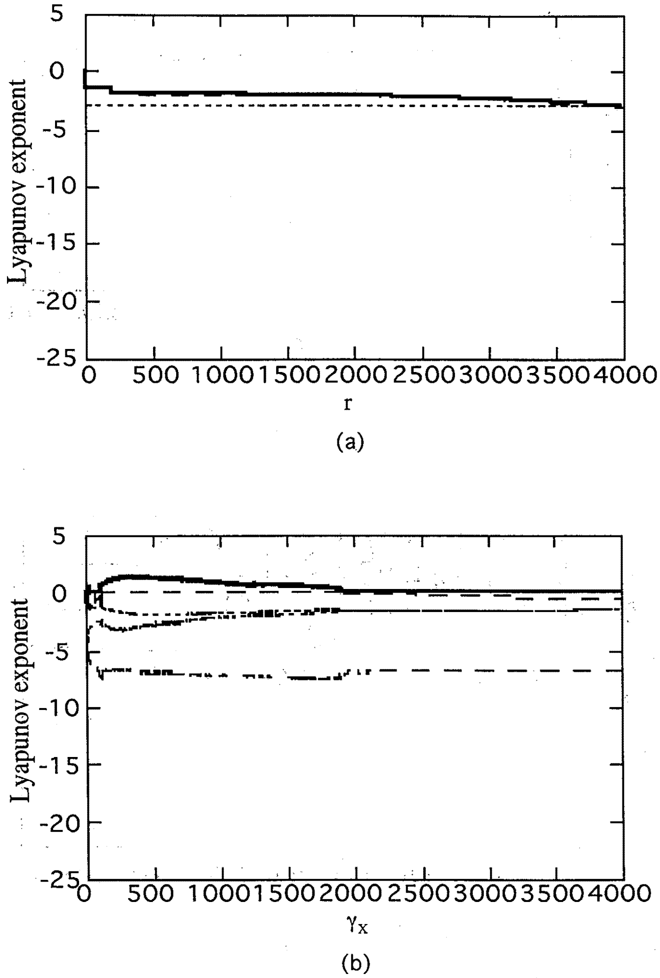


Fig. 3.15 The relation between the Lyapunov exponent and $r$ or $\gamma_X$ for $P_r=1.0$.
(a) the three components model
(b) the five components model

as the period-doubling process of the solution. Finally, for the regime of $\gamma_X >$ 2200 the five components model also falls into the limit cycle with zero value of the exponent. The stability of the limit cycle in extremely large Rayleigh number regime is discussed in Ref. [23]. Detailed structure of the solution corresponding to the case studied here is illustrated in the lower level of the lines in Fig. 3.3.

For the reference, the Lyapunov exponent is calculated changing the parameters $r$ and $\gamma_X$ for the case with $P_r=1.0$ and is shown in Figure 3.15. For the three components model, all the Lyapunov exponents are negative for any value of $r$ as is seen in Fig. 3.15(a), which means that the fixed points are always stable. On the other hand, in the five components model the chaos and limit cycle appear in the presence of the positive value of the exponent, but finally the exponent becomes zero. The result is shown in Fig. 3.15(b).

Now let us investigate the difference between the three components model and the five components one. We here concentrate on the non-linearity term $VW$ in Eq. (3.10) in the five components model. Because the main difference between the three components model and the five components one lies in the term $VW$. The variables $V$ and $W$ depend on the variable $X$.

We introduce a new parmeter $\delta$ into Eq. (3.10), that is,

$$\frac{dX}{d\tau}=\delta VW+P_r(Y-X), \tag{3.25}$$

where $0<\delta\leq 1$. We shall investigate the Lyapunov exponent and the trajectory of the solution in the phase space by changing the value of $\delta$.

The Lyapunov exponent is calculated for various values of $\delta$ for the case with $\gamma_X=400.0$, and the result is shown in Figure 3.16. It is seen from this figure that the existence of the term $\delta VW$ in Eq. (3.25) does not affect the values of the

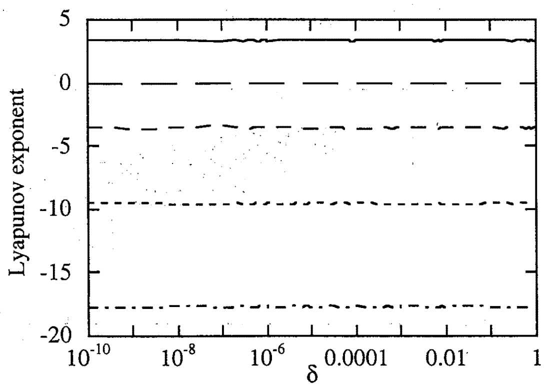


Fig. 3.16 Lyapunov exponent v.s. $\delta$ for $\gamma_X=400.0$ (the five components model)

Lyapunov exponents. For the parameter $r = \gamma_X = 400.0$, the three components model has a limit cycle and the five components model has a chaotic attractor (Fig. 3.10), where the maximum Lyapunov exponents are zero and 3.36, respectively. The trajectory in the phase space projected onto the $V-W$ plane is shown in Figure 3.17 for various values of $\delta$. The variables $X$, $Y$ and $Z$ do not affect their amplitudes. The amplitudes of $V$ and $W$ become larger as the value of $\delta$ becomes smaller, so that the amplitude of the term $\delta VW$ is found to be constant.

For the case with $\gamma_X = 1380.0$, where the five components model has a chaotic solutions and the three components model has a periodic ones in this

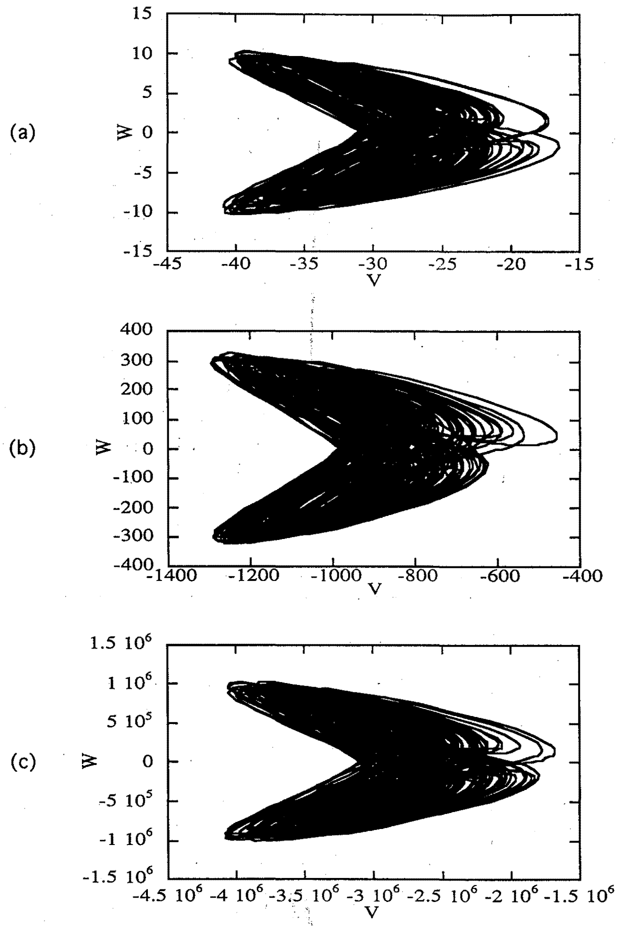


Fig. 3.17 Trajectory phase space projected to $V-W$ plane in the case with $\gamma_X = 400.0$
(a) $\delta = 1.0$ (b) $\delta = 1.0 \times 10^{-3}$ (c) $\delta = 1.0 \times 10^{-10}$

parameter regime, we also obtain similar results, i. e., the Lyapunov exponent are not affected by the change of $\delta$, while the amplitudes of $V$ and $W$ depend on the change of $\delta$. It suggests that in the limit of $\delta \to 0$ the five components model has a kind of sigularity and does not reduce to the three components model.

Finally we present the numerical result of the Nusselt number, which corresponds to the heat flux, in order to study a statistical quantity. The Nusselt number $N_u$ is defined by the ratio of the total transport consisting of the conduction part and the convection part to the conduction part as,

$$N_u = 1 + \frac{\langle p v_x \rangle}{\chi \kappa}, \tag{3.26}$$

where $\langle \ \rangle$ stands for the space average. Setting $q = \pi$ and using Eqs. (2.32), (3.24), (2.34), (2.35) and (3.26),

$$N_u = 1 + \frac{\overline{XY}}{r} \tag{3.27}$$

is obtained for the three components model, where $\overline{\phantom{x}}$ means the time average. Similarly we obtain

$$N_u = 1 + \frac{\overline{XY}}{\gamma_X} \tag{3.28}$$

for the five components model. Figure 3.18 shows the relation between $N_u$ and $r$ (a) or $\gamma_X$ (b) by the symbol 'o' for $P_r = 4.0$. A jump between $r = \gamma_X = 20$ and 30 is due to the bifurcation from the fixed point to the chaotic attractor at $r = \gamma_X = 29$. The difference of the Nusselt number between the limit cycle and the chaotic attractor is not be discussed, because error-bars are extremely large. We can only mention that we do not see any difference between the two models. We present Figure 3.19 in order to show the reason why the error-bars are so large. Figure 3.19 shows the variation of standard deviation $\sigma_{N_u}$ with $r$ (a) or $\gamma_X$ (b). The large error-bars are found to be caused by the increase of the value $\sigma_{N_u}$ as $\sigma_{N_u} \propto r^{0.42}$ or $\sigma_{N_u} \propto \gamma_X{}^{0.42}$. The size of the attractor becomes large with the increase of $r$ or $\gamma_X$, regardless of the kind of the attractors.

### 3.3 Analysis of Intermittency for Three and Five Components Models

In this section, we analyze the intermittency observed in our numerical calculation. According to the review given in Sec. 2.5, the simple categorization of the intermittency is summarized as follows: The Type I intermittency has the characteristic that the duration of laminar phases $\tau$ diverges like $\tau \sim 1/\sqrt{\varepsilon}$ and the Lyapunov exponent obeys the law $\lambda(\varepsilon) \sim \sqrt{\varepsilon}$, where $\varepsilon = r - r_i$ (for the three components model) or $\varepsilon = \gamma_X - \gamma_{X_i}$ (for the five components model). Here $r_i$ and $\gamma_{X_i}$ represent the intermittency thresholds, respectively. The Type III intermittency has a scaling law $\tau \sim 1/\varepsilon$ and $\lambda(\varepsilon) \sim \varepsilon$. In our model, the Type II intermittency does not exist from the definition, therefore we concentrate our analysis on whether the observed intermittency belongs to the Type I, the Type

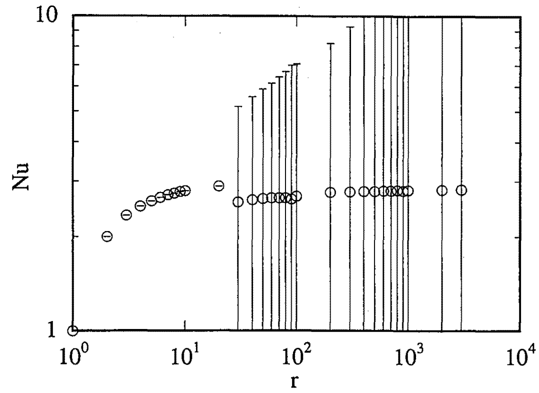


(a)

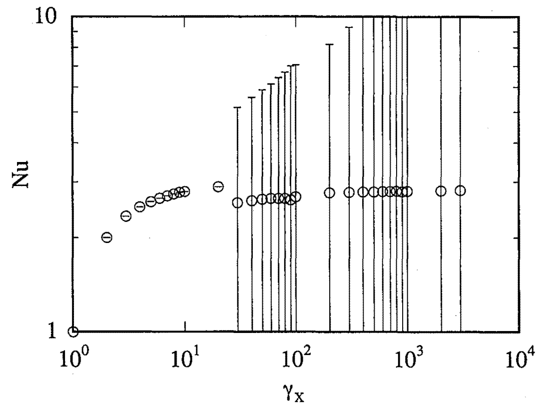


(b)

Fig. 3.18 Log-log plot of the Nusselt number $Nu$ and the normalized Rayleigh number $r$ or $\gamma_x$ is shown by ○ and the error bars are also plotted for Pr=4.0.
(a) the three components model
(b) the five components model

III or else.

Firstly, we investigate the intermittent behaviors of the solutions near $r=\gamma_X=82$ for both the three and the five components models. In these cases, the intermittency thresholds are given by the calculation to be $r_i=\gamma_{X_i}=82.73457$, which is determined according to the maximum Lyapunov exponent being closest to zero. We show the results obtained for the three components model, since the results from the five components model show the similar behavior to

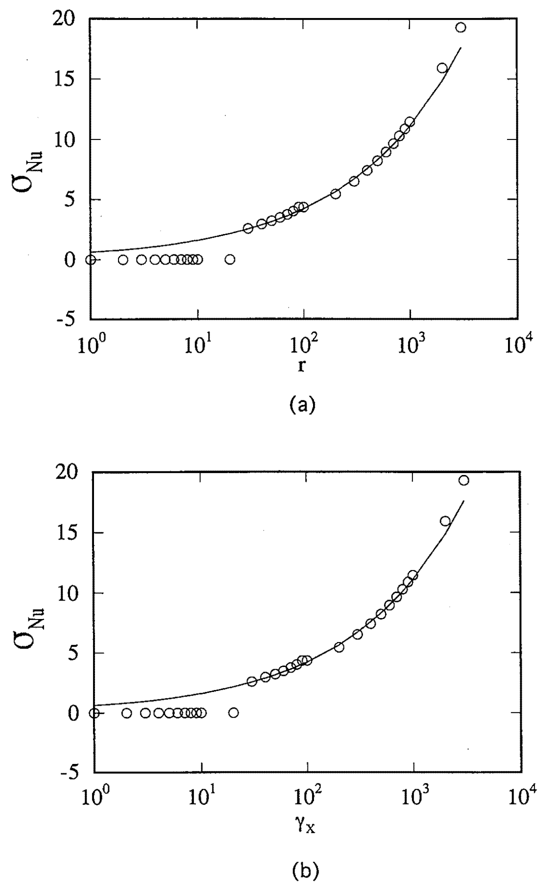


Fig. 3.19 Standard deviation of $Nu$, $\sigma_{Nu}$, v.s. $r$ and $\gamma_x$. The solid line is $\sigma_{Nu}=0.61r^{0.42}$ for (a) and $\sigma_{Nu}=0.61\gamma_X^{0.42}$ for (b).
(a) the three components model
(b) the five components model

those from the three components model, if the condition $\gamma_X<140$ is satisfied as is discussed in Sec. 3.2. We study the scaling law of the duration of laminar phases $\tau$ and the maximum Lyapunov exponent $\lambda(\varepsilon)$. We calculate $\tau$ for 200 cases by changing the initial value randomly with fixed value of $r=82.73457$ or $\varepsilon=0.01$. Figure 3.20 (a) shows the distribution $P(\gamma, \varepsilon)$ of the duration of the laminar phases $\tau$. The peak value of $\tau\sim50$ is observed, while the value is obtained by the theoretical estimation as $\tau\sim1/\sqrt{\varepsilon}=10$ for the Type I intermittency and $\tau\sim1/\varepsilon=100$ for the Type III intermittency.

The relation of $\lambda(\varepsilon)$ and $\varepsilon$ is also calculated and is shown in Fig. 3.20(b).

From the theoretical estimation, we have the scaling law of $\lambda$ which is $\lambda(\varepsilon)\sim\sqrt{\varepsilon}$ if it is the Type I intermittency. The slope is approximately given by 0.4, which is close to the theoretical prediction, i. e., 0.5. However, the fit to $\lambda\sim\varepsilon$ is also statistically admissible, this fact reserves a possibility for the Type III.

Let us next try to identify the type of intermittency observed near $\gamma_X=1345$ for the five components model (Sec. 3.2Case (4)). In this case, the intermittency threshold is calculated to be $\gamma_{X_t}=1345.16784$ from the $\gamma_{X_t}$ survey. The time evolution of $Y$ is shown in Fig. 3.13. The scaling law of the duration of laminar phases $\tau$ is estimated. We calculate $\tau$ for 217 cases by changing the initial value with fixed value of $\gamma_X=1345.17784$, which corresponds to the case of $\varepsilon=0.01$. The distribution $P(\tau,\ \varepsilon)$ of the duration of laminar phases $\tau$ is obtained and is shown in Figure 3.21(a). This figure indicates the peak value of $\tau$ around $\sim 150$. The peak value has been obtained by the theoretical estimation for the Type III intermittency as, $\tau\sim 1/\varepsilon=100$. We find a rough agreement of the value between the theoretical prediction and our numerical result. However, the profile does not have a tail component which is also typical characteristic of the Type III intermittency (Fig. 2.5). The profile is similar to the Type I intermittency rather than the Type III (Fig. 2.4).

The second analysis of the Type I or III intermittency is done by obtaining the relation between the Lyapunov exponent $\lambda(\varepsilon)$ and the difference from intermittency threshold $\gamma_{X_t}$, i. e. $\varepsilon$. We calculate $\lambda$ by changing the value of $\varepsilon$ from $10^{-5}$ to $10^{-1}$. Figure 3.21(b) shows log-log plot of $\lambda(\varepsilon)$ versus $\varepsilon$. According to the thoretical prediction, a scaling law of $\lambda$ is given by $\lambda(\varepsilon)\sim\varepsilon$ if it is the Type III. Namely, the slope of the line interpolating data points should be unity. The simulation results show that the slope is roughly $\approx 0.4$. This result is closer to a theoretical estimation predicted for the Type I rather than that for the Type III. However, either the Type I or the Type III is statistically admissible. We do not draw a decisive conclusion due to the large error bars.

We may need more sample data for the statistical accuracy and to check whether the profile has a tail or not with respect to calculating the distribution $P(\gamma,\ \varepsilon)$. This is left for future work. At this stage of our analysis, the decisive conclusion to classify the Types of the intermittency is not obtained.

Let us discuss the reasons why the decisive conclusion in the scaling law of the Lyapunov exponent $\lambda(\varepsilon)$ is not made. One reason is that our numerical simulation may not be accurate. The other is that the Lyapunov exponent converges so slowly with the time step that it is difficult to estimate the exponent accurately. Near the intermittency threshold [11] , the time evolution is not perfectly periodic oscillation. If a system is periodic, theoretically the maximum Lyapunov exponent is zero. In our simulation at the intermittency threshold $\gamma_{X_t}$, the Lyapunov exponent is not zero but has the finite value $\lambda=0.0543$. This may cause an inaccuracy.

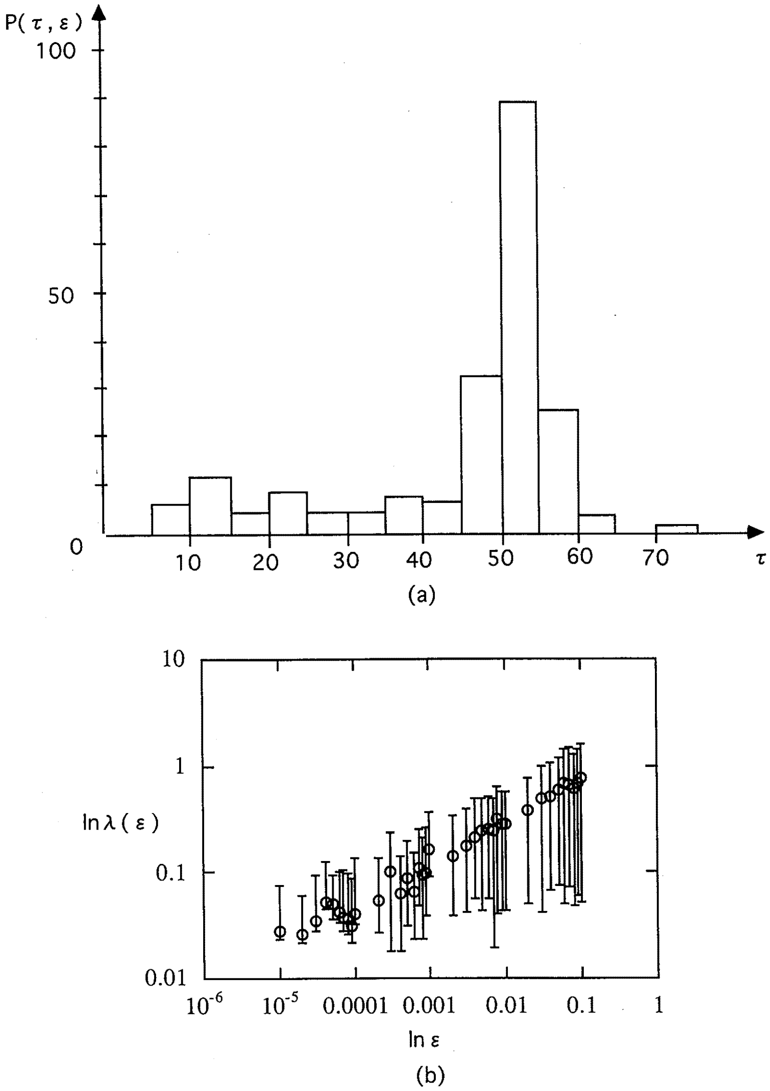


Fig. 3.20 (a) Distribution $P(\tau, \varepsilon)$ of duration of laminar phases $\tau$.
(b) Log-log plot of the Lyapunov exponent $\lambda$ and $\varepsilon$.

## § 4. Summary and Discussion

Numerical simulations of the three components Lorenz model and of the five components model are performed with respect to the behavior of the solutions, the power spectrum and the heat flux. The results are compared with

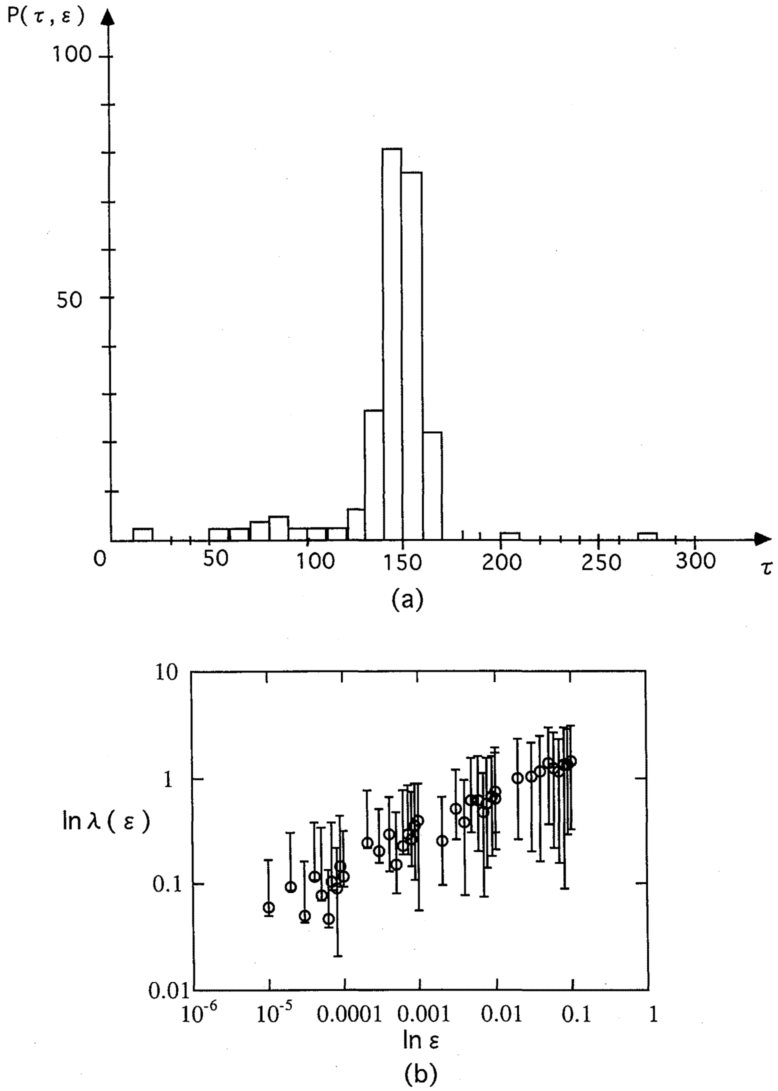


Fig. 3.21 (a) Distribution $P(\tau, \varepsilon)$ of duration of laminar phases $\tau$.
(b) Log-log plot of the Lyapunov exponent $\lambda$ and $\varepsilon$.

each other based on the analysis using the Lyapunov exponent. Parameter surveys are done with respect to the normalized Rayleigh numbers, $\gamma_X$ for the five components model and $r$ for the three components model, respectively.

The results for the case with $P_r=4.0$ are summarized and shown in Fig. 3. 3. It is found that the solution of the five components model has also the fixed point, the limit cycle, the period-doubling bifurcation, the intermittent behavior and the chaotic attractor. Comparing the results of the five components model with those of the three components model, both results show the similar behaviors with respect to time evolution of the solution, the structure of the power spectrum and the cahotic attractor in the regime of $r=\gamma_X<140$. In this regime, the maximum Lyapunov exponents for both models agree with each other. When $r$ is largher than 140, the solution of the three components model falls into a limit cycle (the periodic oscillation). On the other hand that of the five components model has both the limit cycle and the chaotic attractor for $\gamma_X>140$. We presented the chaotic behavior by using the plots on the phase space, the time evolution, the power spectrum and the relation between the Lyapunov exponent and the control parameter (Rayleigh number).

As the normalized Rayleigh number ($r$ or $\gamma_X$) becomes larger, namely as the turbulence is developed, the turbulent structure may not be described without introducing many degrees of freedom. The three components may not be enough to describe a chaos in the regime of higher Rayleigh number or of well developed turbulence. We examine the five components case in this article. However the six components model or the seven components model has been already proposed for the extended Lorenz model with the shear flow effect [24, 25, 26]. A model with a small number of degree of freedom, such as three, five, six [24, 25], and seven models [26], has the limit to describe a chaos. The model adopted in this paper can apply only to a certain extent of the Rayleigh number. At present, we could not explore the boundary limit. Inter-relation between a model with small number of degree of freedom and that with intermediate of large number of degree of freedom should be investigated for future.

We also studied both models for the case with $P_r=1.0$. The numerical analysis for the Lyapunov exponent is shown in Figure 3.15. In the three components model, only the negative Lyapunov exponent is obtained, which means that the fixed point is linearly stable. On the other hand, in the five components model, the fixed point, the limit cycle, the period-doubling bifurcation, the intermittency and the chaotic attractor are observed.

To illustrate the relation between the attractor and the control parameters such as the Rayleigh number and the Prandtl number, we show the behavior of attractor on $P_r$-$r$ plane for the three components model (Figure 4.1) and on the $P_r$-$\gamma_X$ plane for the five components model (Figure 4.2). As for the five components model with $P_r=1.0$, the period-doubling bifurcation occurs near the value of $\gamma_X\approx20$.

Furthermore we analyzed the intermittency and tried to identify the type of the observed intermittency. The intermittencies near $r=\gamma_X=82$ for both the three components model and for the five components model were analyzed. Both the scaling law of the duration of laminar phases $\tau$ (Fig. 3.20(a)) and the scaling law of the Lyapunov exponent $\lambda$ (Fig. 3.20(b)) do not exclude the possibility that it is the Type I or the Type III. The conclusion was not obtained.

The intermittent behavior near the value $\gamma_X=1345$ is studied for the five components model. The scaling law of the duration of laminar phases $\tau$ is investigated in order to identify this intermittency (Fig. 3.21(a)). Both the Type I and III intermittencies are statistically admissible (Fig. 3.21(b)). We could not draw the conclusion.

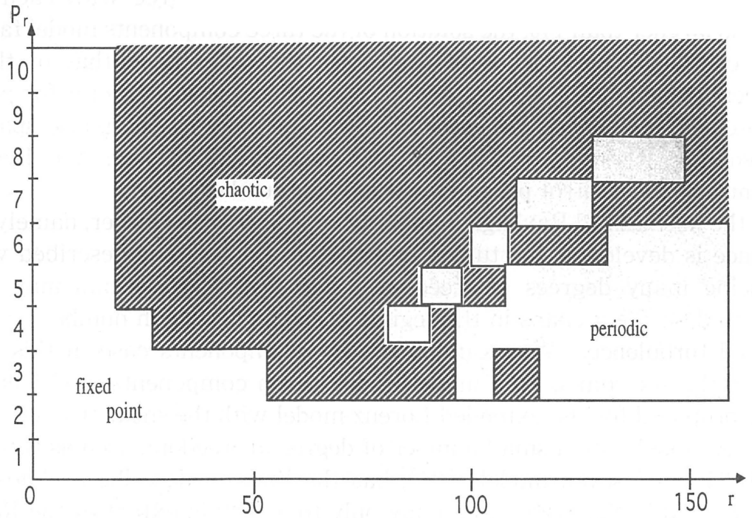


Fig. 4.1 The behavior of solution due to the relation of Prandtl number $Pr$ and normalized Rayleigh number $r$ for the three components model.

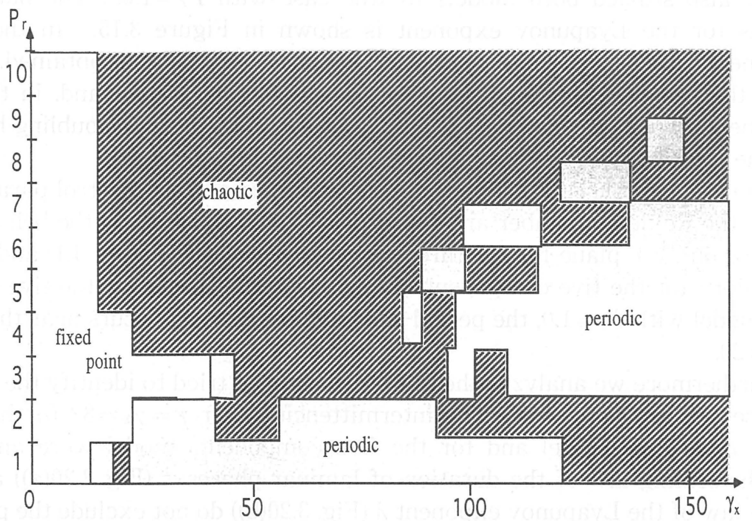


Fig. 4.2 The behavior of solution due to the relation of Prandtl number $Pr$ and normalized Rayleigh number $\gamma_x$ for the five components model.

The ambiguity comes from the numerical inaccuracy. Especially, the fluctuation of the Lyapunov exponent near the intermittency threshold makes it difficult to have enough accuracy in the numerical simulations. We also do not have enough statistical accuracy to obtain the decisive conclusion from our analysis. To improve our simulation code and to increase the statistical accuracy is left for future work.

## Acknowledgement

The authors with to thank Profs. M. Wakatani and Z. Yoshida for the creative comments, and Drs. H. Sugama and A. Takayama for fruitful suggestions. They also would like to acknowledge for the Messrs. S. Toda and T. Kubota for fruitful discussions. Furthermore one of the authors (T. A.) expresses thanks to his parents, Mr. T. Aoyagi and Mrs. K. Aoyagi for their support.

## References

[1] S. Nishikawa and H. Yahata: J. Phys. Soc. Jpn. **65** 935 (1995).
[2] E. N. Lorenz: J. Atmos. Sci. **20** 130 (1963).
[3] C. Boldrighini and V. Franceschini: Commun. Math. Phys. **64** 159 (1979).
[4] J. Crutchfield, D. Farmer, N. Packard, R. Shaw, G. Jones and R. J. Donnelly: Phys. Lett. **76** (1980).
[5] P. Bergē, Y. Pomeau and C. Vidal: "Order within chaos", John Wiley & Sons (1984).
[6] L. D. Landau: Akad. Nauk. Doklady **44** 339 (1944).
[7] D. Ruelle and F. Takens: Commun. Math. Phys. **20** 167 (1971).
[8] J. Froyland and K. H. Alfsen: Phys. Rev. A **29** 2928 (1984).
[9] T. Nagashima and I. Shimada: Prog. Theor. Phys. **58** 1318 (1977).
[10] A. Wolf, J. B. Swift, H. L. Swinney and J. A. Vastano: Physica 16D 285 (1985).
[11] Y. Pomeau and P. Manneville: Commun. Math. Phys. **74** 189 (1980).
[12] M. Dubois, M. A. Rubio and P. Berge: Phys. Rev. Lett. **51** 1446 (1983).
[13] G. Mayer-Kress and H. Haken: Physica 10D 329 (1984).
[14] N. Morioka and T. Shimizu: Phys. Lett. **66A** 447 (1978).
[15] H. Dido: Prog. Theor. Phys. **70** 879 (1983).
[16] O. Pogutse, W. Kerner, V. Gribkov, S. Bazdenkovn and M. Osipenko: Plasma Phys. Control. Fusion **36** 1963 (1994).
[17] N. N. Kukharkin, M. V. Osipenko, O. P. Pogutse and V. M. Gribkov: Proc. 14th IAEA Conference on Plasma Physics and Controlled Nuclear Fusion Research **2** 293 (1992).
[18] S. V. Bazdenkov and O. P. Pogutse: JETP Lett. **57** 410 (1993).
[19] A. Takayama: master thesis (1995).
[20] A. Takayama, M. Wakatani and H. Sugama: J. Phys. Soc. Jpn. **64** 791 (1995).
[21] H. Sugama and M. Wakatani: J. Phys. Soc. Jpn. **59** 3937 (1990).
[22] P. Manneville and Y. Pomeau: Physica 1D 219 (1980).
[23] E. A. Jackson: "Perspective of Nonlizear Dynamics II", Cambridge University Press (1991).
[24] L. N. Howard and R. Krishnamurti: J. Fluid Mech. **170** 385 (1986).
[25] W. Horton, G. Hu and G. Laval: Phy. Plasmas. **3** 2912 (1996).

[26] J. L. Thiffeault and W. Horton: Phys. Fluid 8 1715 (1996).

(Received May 8, 1997)